











Research Paper

The Evolutionary Map of the Universe pilot survey

Ray P. Norris^{1,2,*} , Joshua Marvil^{2,3}, J. D. Collier^{1,2,4}, Anna D. Kapińska³, Andrew N. O'Brien^{1,2,5}, L. Rudnick⁶ , Heinz Andernach⁷, Jacobo Asorey⁸, Michael J. I. Brown⁹, Marcus Brüggen¹⁰, Evan Crawford¹ , Jayanne English¹¹, Syed Faisal ur Rahman¹², Miroslav D. Filipović¹, Yjan Gordon¹¹, Gülay Gürkan^{13,14} , Catherine Hale^{13,15} , Andrew M. Hopkins^{1,16}, Minh T. Huynh¹³, Kim HyeongHan¹⁷, M. James Jee^{17,18}, Bärbel S. Koribalski^{1,2}, Emil Lenc² , Kieran Luken^{1,2}, David Parkinson^{19,20} , Isabella Prandoni²¹, Wasim Raja², Thomas H. Reiprich²², Christopher J. Riseley^{13,21,23}, Stanislav S. Shabala²⁴, Jaimie R. Sheil⁹, Tessa Vernstrom¹³, Matthew T. Whiting², James R. Allison^{2,25}, C. S. Anderson^{2,3} , Lewis Ball^{2,26}, Martin Bell^{2,27}, John Bunton², T. J. Galvin^{1,13,28}, Neeraj Gupta^{2,29}, Aidan Hotan¹³ , Colin Jacka², Peter J. Macgregor^{1,2} , Elizabeth K. Mahony², Umberto Maio³⁰, Vanessa Moss², M. Pandey-Pommier³¹ and Maxim A. Voronkov²

¹Western Sydney University, Locked Bag 1797, Penrith, NSW 2751, Australia, ²CSIRO Space & Astronomy, P.O. Box 76, Epping, NSW 1710, Australia, ³National Radio Astronomy Observatory, PO Box 0, Socorro, NM87801, USA, ⁴The Inter-University Institute for Data Intensive Astronomy (IDIA), Department of Astronomy, University of Cape Town, Rondebosch, 7701, South Africa, ⁵Department of Physics, University of Wisconsin-Milwaukee, P.O. Box 413, Milwaukee, WI 53201, USA, ⁶Minnesota Institute for Astrophysics, University of Minnesota, 116 Church St. SE, Minneapolis, MN 55455, USA, ⁷Depto. de Astronomía, DCNE, Universidad de Guanajuato, Cjón. de Jalisco s/n, Guanajuato, CP 36023, Mexico, ⁸Centro de Investigaciones Energéticas, Medioambientales y Tecnológicas (CIEMAT), Av. Complutense, 40, 28040 Madrid, Spain, ⁹School of Physics and Astronomy, Monash University, Clayton, VIC 3800, Australia, ¹⁰University of Hamburg, Hamburger Sternwarte, Gojenbergsweg 112, 21029 Hamburg, Germany, ¹¹Institute of Space and Planetary Astrophysics (ISPA), University of Karachi (UoK), Karachi, Pakistan, ¹²Department of Physics and Astronomy, University of Manitoba, Winnipeg, MB R3T 2N2, Canada, ¹³CSIRO Space & Astronomy, PO Box 1130, Bentley WA 6102, Australia, ¹⁴Thüringer Landessternwarte, Sternwarte 5, D-07778 Tautenburg, Germany, ¹⁵School of Physics and Astronomy, Institute for Astronomy, University of Edinburgh, Royal Observatory, Blackford Hill, EH9 3HJ Edinburgh, UK, ¹⁶Australian Astronomical Optics, Macquarie University, 105 Delhi Rd, North Ryde, NSW 2113, Australia, ¹⁷Yonsei University, Department of Astronomy, Seoul, Republic of Korea, ¹⁸Department of Physics, University of California, Davis, California, USA, ¹⁹Korea Astronomy and Space Science Institute, Daejeon 34055, Korea, ²⁰University of Science and Technology, Daejeon 34113, Korea, ²¹INAF – Istituto di Radioastronomia, via P. Gobetti 101, 40129 Bologna, Italy, ²²Argelander Institute for Astronomy (Alfa), University of Bonn, Auf dem Hügel 71, 53121 Bonn, Germany, ²³Dipartimento di Fisica e Astronomia, Università degli Studi di Bologna, via P. Gobetti 93/2, 40129 Bologna, Italy, ²⁴School of Natural Sciences, University of Tasmania, Private Bag 37, Hobart, TAS 7001, Australia, ²⁵Sub-Dept. of Astrophysics, Department of Physics, University of Oxford, Denys Wilkinson Building, Keble Rd., Oxford, OX1 3RH, UK, ²⁶SKA Observatory, Jodrell Bank, Lower Withington, Macclesfield, Cheshire SK11 9FT, UK, ²⁷School of Mathematical and Physical Sciences, University of Technology Sydney, ²⁸International Centre for Radio Astronomy Research, Curtin University, Bentley, WA 6102, Australia, ²⁹IUCAA, Post Bag 4, Ganeshkhind, Pune University Campus, Pune 411 007, India, ³⁰INAF - Observatory of Trieste, via G. Tiepolo 11, 34143 Trieste, Italy and ³¹University Claude Bernard Lyon 1, Bâtiment Quai 43 - 2ème étage, 28, avenue Gaston Berger, 69622 Villeurbanne Cedex, France

Abstract

We present the data and initial results from the first pilot survey of the Evolutionary Map of the Universe (EMU), observed at 944 MHz with the Australian Square Kilometre Array Pathfinder (ASKAP) telescope. The survey covers 270 deg² of an area covered by the Dark Energy Survey, reaching a depth of 25–30 μJy beam⁻¹ rms at a spatial resolution of ~11–18 arcsec, resulting in a catalogue of ~220 000 sources, of which ~180 000 are single-component sources. Here we present the catalogue of single-component sources, together with (where available) optical and infrared cross-identifications, classifications, and redshifts. This survey explores a new region of parameter space compared to previous surveys. Specifically, the EMU Pilot Survey has a high density of sources, and also a high sensitivity to low surface brightness emission. These properties result in the detection of types of sources that were rarely seen in or absent from previous surveys. We present some of these new results here.

Keywords: Extragalactic astronomy – Radio astronomy – Sky surveys

(Received 13 May 2021; revised 29 July 2021; accepted 30 July 2021)

* Author for correspondence: Ray P. Norris, E-mail: raypnorris@gmail.com

Cite this article: Norris RP, Marvil J, Collier JD, Kapińska AD, O'Brien AN, Rudnick L, Andernach H, Asorey J, Brown MJI, Brüggen M, Crawford E, English J, Rahman SF, Filipović MD, Gordon Y, Gürkan G, Hale C, Hopkins AM, Huynh MT, HyeongHan K, Jee MJ, Koribalski BS, Lenc E, Luken K, Parkinson D, Prandoni I, Raja W, Reiprich TH, Riseley CJ, Shabala SS, Sheil JR, Vernstrom T, Whiting MT, Allison JR, Anderson CS, Ball L, Ball M, Bunton J, Galvin TJ, Gupta N, Hotan A, Jacka C, Macgregor PJ, Mahony EK, Maio U, Moss V, Pandey-Pommier M and Voronkov MA. (2021) The Evolutionary Map of the Universe pilot survey. *Publications of the Astronomical Society of Australia* 38, e046, 1–26. <https://doi.org/10.1017/pasa.2021.42>

1. Introduction

Large radio surveys provide substantial samples of galaxies for studying cosmology. They also reveal rare but important stages of galaxy evolution and expand the volume of observed parameter space. Before the survey described here took place, about 2.5 million radio sources were known. That figure is about to increase by about two orders of magnitude (Norris 2017a), primarily due

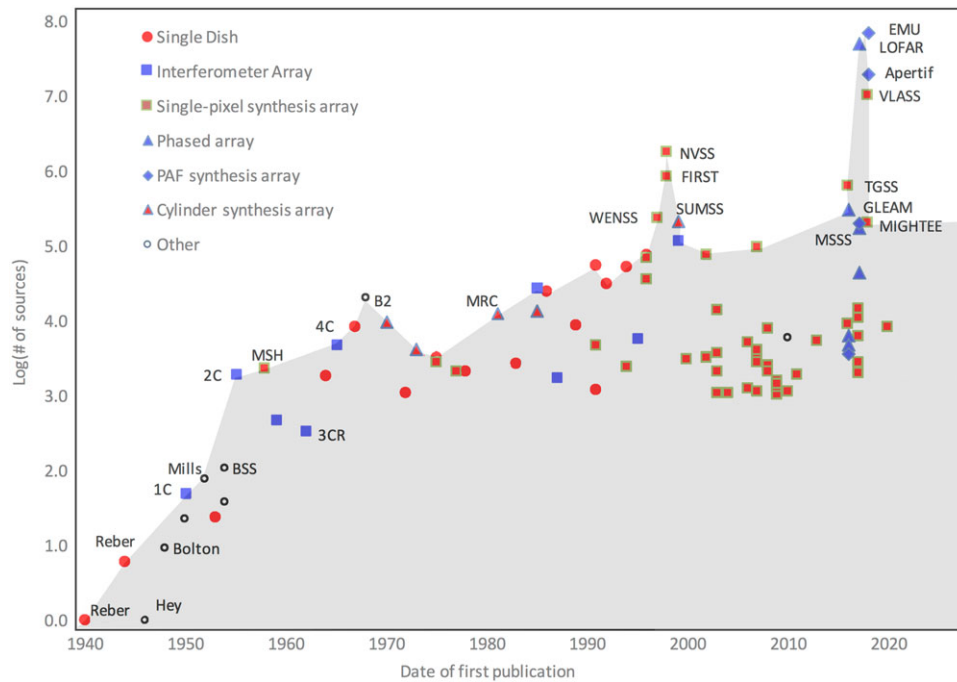


Figure 1. The number of known extragalactic radio sources discovered by surveys as a function of time, adapted from Norris (2017a). The symbols indicate the type of telescope used to make the survey, and are fully described in Norris (2017a). The dates and survey size are based on estimates made in 2017, and some later surveys (e.g. RACS McConnell *et al.* 2020, with 2.8 million sources) are missing from this plot. Survey abbreviations and references are given in Norris (2017a). The shading under the curve is merely to improve readability.



Figure 2. Some of the ASKAP antennas equipped with phased array feeds, located in the Murchison Region of Western Australia. Photo credit: CSIRO

to using innovative technology in the development of new radio telescopes and upgrading of older radio telescopes. These technological developments will enable several large radio surveys, which are expected to drive a rapid advance in knowledge. Figure 1 shows the historical growth of these surveys.

One of these new telescopes is the Australian Square Kilometre Array Pathfinder, (ASKAP, Johnston *et al.* 2007; Johnston *et al.* 2008; McConnell *et al.* 2016; Hotan *et al.* 2021) which consists of 36 12-m antennas spread over a region 6 km in diameter at the Murchison Radio-astronomy Observatory in Western Australia, shown in Figure 2. At the focus of each antenna is an innovative phased-array feed (PAF: Hay *et al.* 2006) of 94 dual-polarisation pixels (Figure 3). As a result, ASKAP has an instantaneous field



Figure 3. One of the phased array feeds. Each square on the chequerboard is an antenna element connected to two receivers. Photo credit: CSIRO

of view up to 30 deg^2 , producing a much higher survey speed than that of previous synthesis arrays. The antennas are a novel three-axis design, with the feed and reflector rotating to ensure a constant position angle of the PAF and sidelobes on the sky.

The first all-sky survey undertaken by ASKAP was the Rapid ASKAP Continuum Survey (McConnell *et al.* 2020) which surveyed the entire sky south of Declination $+41^\circ$ to a median rms of about $250 \mu\text{Jy beam}^{-1}$. Apart from its astrophysical importance, this survey will also generate a sky model (Hale *et al.*, in preparation) to facilitate the calibration of subsequent deeper observations with ASKAP.

ASKAP will conduct a deep all-sky continuum survey known as the Evolutionary Map of the Universe (EMU: Norris *et al.* 2011). The primary goal of EMU is to make a deep ($10\text{--}20 \mu\text{Jy beam}^{-1}$ rms) radio continuum survey of the entire southern sky, extending

Table 1. EMU Pilot Survey specifications.

| | |
|-------------------------|---|
| Area of survey | 270 deg ² |
| Synthesised beamwidth | Typically 13 arcsec × 11 arcsec FWHM |
| Frequency range | 800 – 1088 MHz |
| Observing configuration | ‘closepack36’ with pitch 0.9° and no interleaving |
| Total integration time | 10 × 10 h |

as far north as +30°. EMU is expected to generate a catalogue of as many as 70 million galaxies.

In preparation for the full EMU survey, we conducted the EMU Pilot Survey (EMU-PS) with the goal of testing the planned EMU survey strategy and the processing pipeline. In designing the pilot survey, we adopted the following boundary conditions:

- Declination < −30° (to avoid potentially poor u, v coverage near the equator).
- Galactic latitude > +20° (to avoid the strong diffuse emission in the Galactic plane).
- Sufficiently far from the Sun to avoid solar interference, or night-time observation.
- A single area of 240–300 deg², of 10–12 h observations each on contiguous fields, to form a rectangular area. Cosmological analyses are optimised if the area is as square as possible.
- Fields overlapped by a small amount to provide uniform sensitivity.
- Frequency band chosen to avoid any radio frequency interference and maximise survey speed, subject to constraints on resolution and confusion.
- Field that is well studied at other wavelengths to maximise the scientific value.

These boundary conditions were satisfied by the survey described in this paper. The survey specifications are given in [Table 1](#).

An area of sky within the Dark Energy Survey (DES; Abbott et al. 2018) was chosen so that we could access the excellent optical photometric data available from DES. EMU and DES have a Memorandum of Understanding that enables data to be shared between the two projects.

The observations were taken and processed in late 2019. It should be emphasised that, at the time of observation, commissioning of the telescope and its processing software were not yet complete, so that there are known telescope issues and processing deficiencies which were not yet addressed. As a result, the images show some artefacts, and the rms noise level is about twice as high as we expect in the final EMU survey. Nevertheless, this is still the largest radio survey ever completed at this depth, and so a great deal of valuable science results are being obtained, some of which are discussed briefly in this paper.

[Section 2](#) of this paper describes the observations, and [Section 3](#) describes the data reduction. [Section 4](#) describes the ‘value-added’ data processing, and [Section 5](#) presents the results and data access. [Section 6](#) presents some preliminary science results.

1.1. Nomenclature and conventions

Throughout this paper and in the catalogue, we use source names in the format EMU PS JHHMMSS.S–DDMMSS and we define spectral index α in terms of the relationship between flux density S and observing frequency ν as $S \propto \nu^\alpha$.

Table 2. Cosmological parameters used in this paper and adopted for EMU-PS.

| Description | Parameter | value |
|--|---------------------------|--------------|
| Hubble constant | H_0 | 67.36 |
| Matter density | Ω_m | 0.3153 |
| Cosmological constant density | Ω_Λ | 0.6847 |
| Optical depth to reionisation | τ | 0.0544 |
| Physical baryon density | $\Omega_b h^2$ | 0.02237 |
| Physical cold dark matter density | $\Omega_{\text{CDM}} h^2$ | 0.1200 |
| Physical neutrino density | $\Omega_\nu h^2$ | 0.000694 |
| Neutrino hierarchy | 1 massive, two massless | |
| Primordial spectral index of scalar fluctuations | n_s | 0.9649 |
| Amplitude of scalar fluctuations | A_s | $2.055e - 9$ |

Table 3. EMU pilot observation details.

| Date | Field name | RA (J2000) | Dec. (J2000) | Target SBID | Cal SBID | Number of antennas |
|-------------|-------------|-------------|--------------|-------------|----------|--------------------|
| 15 Jul 2019 | EMU_2059-51 | 21:00:00.00 | −51:07:06.4 | 9287 | 9301 | 36 |
| 17 Jul 2019 | EMU_2034-60 | 20:34:17.14 | −60:19:18.2 | 9325 | 9324 | 35 |
| 18 Jul 2019 | EMU_2042-55 | 20:42:00.00 | −55:43:29.4 | 9351 | 9350 | 35 |
| 24 Jul 2019 | EMU_2115-60 | 21:15:25.71 | −60:19:18.2 | 9410 | 9409 | 35 |
| 25 Jul 2019 | EMU_2132-51 | 21:32:43.64 | −51:07:06.4 | 9434 | 9428 | 34 |
| 26 Jul 2019 | EMU_2027-51 | 20:27:16.36 | −51:07:06.4 | 9437 | 9436 | 36 |
| 27 Jul 2019 | EMU_2118-55 | 21:18:00.00 | −55:43:29.4 | 9442 | 9441 | 36 |
| 02 Aug 2019 | EMU_2156-60 | 21:56:34.29 | −60:19:18.2 | 9501 | 9500 | 36 |
| 03 Oct 2019 | EMU_2154-55 | 21:54:00.00 | −55:43:29.4 | 10083 | 10082 | 35 |
| 24 Nov 2019 | EMU_2205-51 | 22:05:27.27 | −51:07:06.4 | 10635 | 10634 | 34 |

The position shown is the antenna pointing centre, corresponding to position (0,0) in [Figure 4](#). Columns 5 and 6 show the ASKAP scheduling block identification (SBID) number for the target and calibrator observations.

For consistency among science results derived from EMU-PS data, we encourage the use of a consistent set of cosmological parameters in papers reporting results from EMU-PS. Here we assume a flat Λ CDM model, with parameter values taken from the mean posterior of the Planck 2018 cosmology, from paper VI (Planck Collaboration et al. 2020), using a combination of Planck data, but with no extra, non-Planck data (e.g. no Baryon Acoustic Oscillation data). This results in the parameter set shown in [Table 2](#).

2. Observations

ASKAP has 36 antennas, all but 6 of which are within a region of 2.3 km diameter, with the outer 6 extending the baselines up to 6.4 km. In all pilot survey observations, as many of the 36 antennas were used as possible. However, in some cases, a few antennas were omitted because of maintenance or hardware issues. The actual number of antennas used is shown in [Table 3](#).

At the prime focus of each antenna is a phased array feed (PAF), which subtends a solid angle of about 30 deg² of the sky. The PAF consists of 188 single-polarisation dipole receivers. A weighted sum of the outputs of groups of these receivers is used to form 36 dual-polarisation ‘beams’. Individual dipole receivers will, in general, contribute to more than one beam, so that adjacent beams are not completely independent. The 36 beams together cover an area of about 30 deg² on the sky, which we refer to as a ‘tile’.

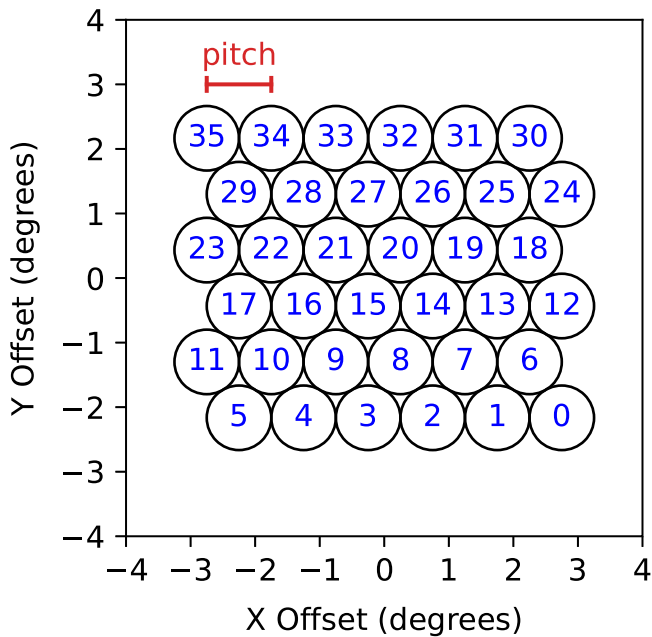


Figure 4. The arrangement of the 36 ASKAP beams in the ‘closepack36’ configuration. The beams are numbered from 0 to 35 (diagram adapted from McConnell *et al.* 2019). The circles shown are for illustration only. For EMU-PS, the actual full width half maximum of each beam is $\sim 1.5^\circ$ at the band centre, and the pitch spacing is 0.9° , giving an approximately uniform sensitivity over the field of view.

There are several ways of arranging the individual beams within the tile. For EMU-PS, we use a hexagonal arrangement of the 36 beams with 6 rows of 6 beams, known as ‘closepack36’ (Hotan *et al.* 2021), shown in Figure 4. This configuration provides more uniform coverage than the widely used rectangular array known as ‘square_6x6’. The spacing between the beams is known as the ‘pitch’ and is set to 0.9° for EMU-PS. In some other ASKAP observations, interleaved observations are taken, with the antenna pointing position shifted by half the pitch, to provide better uniformity. However, this is not necessary for the EMU-PS because of the combination of our lower observing frequency and the closepack36 configuration.

The weights of the individual beams are initially calibrated by observing the Sun, placed successively at the centre of each beam, and then adjusting the weights for maximum signal-to-noise ratio. A radiator at the vertex of each antenna (the On-Dish Calibrator, or ODC) enables the gain of each receiver to be monitored, and the weight solution initially obtained from solar observations may be updated if necessary using these ODC measurements.

Before (or sometimes after) the observation of each target, the calibrator source PKS 1934–638 is observed for 200 s at the centre of each of the 36 beams to provide bandpass and gain calibration. This calibration observation takes about 2 h.

The positions of the tiles are chosen using a tiling scheme which will be used for the main EMU survey, shown in Figure 5. At most declinations, the tiles are aligned with lines of constant declination. At the south polar cap (below declination -71.81°), they are arranged in a rectangular grid as shown in Figure 5. Using this scheme, the sky south of Declination $+30^\circ$ is covered by 1280 tiles. Overlaps between tiles amount to less than 5% of the total area covered.

The pilot survey was observed with ASKAP in the period from 2019 July 15 to 2019 November 24. In some cases, the initial

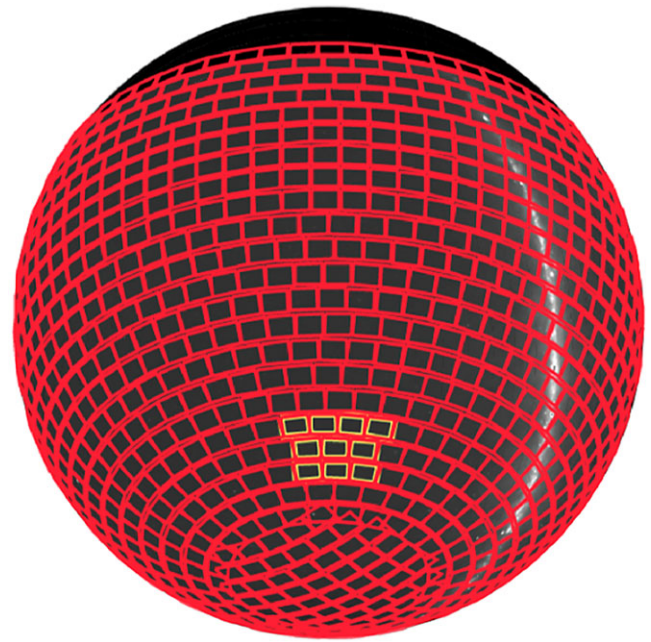


Figure 5. The sky tiling scheme adopted for the EMU-PS. The red rectangles covering the celestial sphere show the tiles planned for the EMU survey, and the orange area indicates the 10 tiles of the EMU-PS. The white strip shows the Galactic plane, and the south celestial pole is at the bottom of the figure.

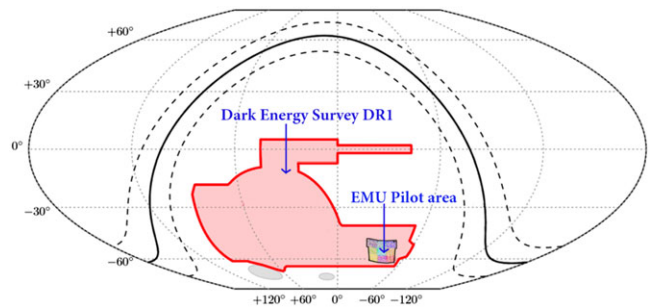


Figure 6. The location of the EMU Pilot Survey area on the sky within DES DR1, adapted from Abbott *et al.* (2018). The diagram is in equatorial coordinates, and the solid line marks the Galactic plane, flanked by two dashed lines showing Galactic latitude $\pm 10^\circ$.

observations were subsequently found to be faulty, in which case the field was re-observed. Table 3 shows the details of the observations that were used in the final data product.

The survey consists of a 10-h observation of each of the 10 tiles, each accompanied by a calibration observation as described above. No further calibration is performed during the observation. The location of the survey area is shown in Figure 6, and the details of the pointing centres are shown in Table 3 and in Figure 7.

3. Pipeline data reduction

We process the data using the ASKAPsoft pipeline (Whiting *et al.* 2017; Whiting 2020; Guzman *et al.* 2019) with the parameters shown in Table 4, and using 2-arcsec square pixels. All parameter names, shown in *italics* in this section, are included in Table 4.

The ASKAP correlator generates 16384 spectral line channels and, for EMU data, we start by averaging these to 288 1-MHz

Table 4. EMU pilot processing parameters. The first column shows the parameter name used by ASKAPsoft.

| Parset name | Explanation | Value |
|--|--|----------------------------|
| DO_SPECTRAL_IMAGING | Only continuum (i.e. 288 1-MHz channels) | false |
| GRIDDER_NWPLANES | Number of w planes | 557 |
| CLEAN_SCALES | Scales used by multiscale CLEAN, in pixels | [0,6,15,30,45,60] |
| CLEAN_NUM_MAJORCYCLES | Number of major cycles of CLEAN | [5,15] |
| CLEAN_THRESHOLD_MINORCYCLE | Stop CLEAN minor cycles at this threshold | [30%, 0.25 mJy, 0.03 mJy] |
| CLEAN_MINORCYCLE_NITER | No. of iterations of CLEAN in each minor cycle | [400, 3 000] |
| SELFCAL_METHOD | Selcal model | CleanModel |
| SELFCAL_INTERVAL | Selcal solution interval (s) in each selfcal iteration | [60] |
| PRECONDITIONER_WIENER_ROBUSTNESS | Briggs robustness parameter in preconditioning | 0.0 |
| RESTORE_PRECONDITIONER_LIST | Use a Wiener filter for the main image and a Gaussian taper for the alt image | [Wiener, GaussianTaper] |
| RESTORE_PRECONDITIONER_WIENER_ROBUSTNESS | Both the main and the alt image have robustness = 0 | 0.0 |
| RESTORE_PRECONDITIONER_GAUSS_TAPER | Taper the ‘alt’ image with a 30 × 30 arcsec Gaussian | [30 arcsec, 30 arcsec, 0°] |
| LINMOS_CUTOFF | Cut off the beams at 0.2 of peak when mosaicing them | 0.2 |
| DO_CONTCUBE_IMAGING | Image using a ‘Continuum cube’? | true |

Table 5. Results of tests to measure the optimum robustness.

| Briggs robustness | bmaj (arcsec) | bmin (arcsec) | rms (I) $\mu\text{Jy beam}^{-1}$ | rms (V) $\mu\text{Jy beam}^{-1}$ |
|-------------------|---------------|---------------|----------------------------------|----------------------------------|
| 2 | 25 | 21 | 46 | 11 |
| 1 | 23 | 19 | 29 | 12 |
| 0.5 | 17 | 14 | 20 | 13 |
| 0 | 13 | 11 | 21 | 16 |
| -0.5 | 9 | 9 | 33 | 29 |
| -1 | 8 | 7 | 56 | 48 |
| -2 | 8 | 7 | 73 | 61 |

Tests were conducted at 888 MHz, using a 10-h ASKAP observation on arrays of 33 (for Stokes V, using SB8129 on a field close to UV Ceti) and 35 (for Stokes I, using SB8137 on the GAMA23 field) antennas. Columns 2 and 3 given the major and minor axes of the restoring beam, and columns 4 and 5 gives the measured rms values in (a) a source-free region of the Stokes I image, and (b) the Stokes V image, which is almost source-free. The results have been scaled to a 10-h observation on an array of 36 antennas.

channels to reduce the computational load (i.e. `DO_SPECTRAL_IMAGING = true` and `DO_CONTCUBE_IMAGING = true`)

Weighting and tapering in ASKAPsoft are done using a Wiener filter preconditioning technique, which is computationally more efficient than traditional tapering and weighting. (i.e. `RESTORE_PRECONDITIONER_LIST = [Wiener, GaussianTaper]`) for the main and alt image respectively

To choose the robustness (Briggs 1995), we conducted tests on part of the GAMA23 field (at about Right Ascension 23:00, Declination -32:00; Leahy et al. (2019), Prandoni et al., in preparation), in both Stokes I (total intensity) and Stokes V (circular polarisation) resulting in the values shown in Table 5. At lower (more negative) values of robustness, the rms increases because the near-uniform weighting discards information. At higher (more positive) values of robustness, corresponding to near-natural weighting, the V rms continues to decrease but the I rms increases presumably because of (a) confusion, (b) poorer u, v coverage leading to increased sidelobes, (c) increased radio frequency interference on short baselines. Based on these results, we

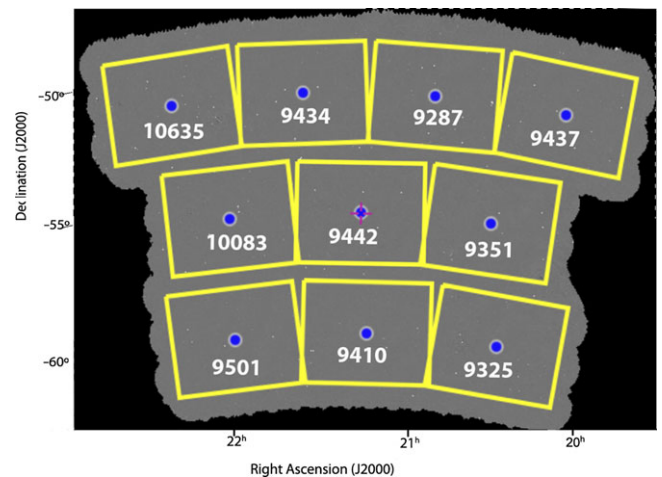


Figure 7. The arrangement of the ten individual ASKAP tiles on the sky for EMU-PS with their SBID numbers as listed in Table 3. The rectangles are separated in this diagram for clarity, but there is actually overlapping coverage as illustrated by the greyscale background.

choose a robustness of 0.0 as an optimum value for the EMU-PS, that is, `PRECONDITIONER_WIENER_ROBUSTNESS = 0.0`. Although robustness +0.5 has a slightly lower rms, it has a significantly increased beam size. No further tapering is used in the main image.

The non-coplanarity of ASKAP is managed using the w-projection technique (Cornwell et al. 2008; Rau et al. 2009), using a total of 557 w-planes (i.e. `GRIDDER_NWPLANES = 557`). The data are gridded using multi-frequency synthesis and deconvolved using a multi-frequency multiscale CLEAN, using `CLEAN_SCALES` of [0,6,15,30,45,60] pixels, which gives 6 scales up to 10 times the clean beam size. After initial imaging and cleaning (using 5 major cycles: `CLEAN_NUM_MAJOR_CYCLES`, with 400 iterations in each minor cycle, down to a limit of 0.25 mJy), the data are given one iteration of phase selfcal using the output of the previous CLEAN (i.e. `SELFCAL_METHOD = CLEAN`) before

the final imaging and cleaning (15 major cycles with up to 3000 iterations in each minor cycle, with minor cycles triggering a major cycle when they reach a 30% CLEAN limit, to a clean limit of $30 \mu\text{Jy}$, i.e. `CLEAN_THRESHOLD_MINORCYCLE`). Two images are produced by the pipeline: the main image at full resolution and an alternative ('alt') image tapered to a 30-arcsec resolution, which is optimised for faint diffuse emission. The alt image is not used in this paper.

The multi-frequency synthesis imaging uses a Taylor term technique (Rau & Cornwell 2011) over the 288-MHz bandwidth to account for the spectral variation of each source. We use two terms in the Taylor expansion, resulting in two planes called TT0 and TT1. The TT0 plane is the zeroth-order term, corresponding to the total intensity of each pixel integrated over the full bandwidth. TT1 is the first-order term and allows the spectral indices at each pixel to be measured as $\alpha = \text{TT1}/\text{TT0}$.

Primary beam correction is applied to each beam, and beams are combined using a weighted mean down to a cut-off of 20% of the peak (i.e. `LINMOSCUTOFF` = 0.2) assuming a Gaussian primary beam shape. Future ASKAP surveys will use a beam shape based on holographic measurements, but that was not available for EMU-PS. Using the Gaussian beam approximation increases calibration errors and the rms noise level.

Source extraction uses the 'Selavy' software tool (Whiting & Humphreys 2012; Whiting et al. 2017) which identifies 'islands' of emission higher than three times the local rms in the image, using a flood-fill technique, and then fits Gaussian components to peaks of emission within the islands. Only components and islands greater than five times the local rms are retained.

In the EMU initial public data release (defined in Section 5.1), spectral indices for individual components are measured as $\alpha = \text{TT1}/\text{TT0}$, where TT0 and TT1 are a weighted mean of the Taylor terms over the area of the component, down to a level of five times the local rms noise. However, this technique has been found to be unsatisfactory, so the spectral indices in the initial public data release should be regarded as unreliable. Our alternative technique is discussed below in Section 4.4

As a final step within the pipeline, the data from each scheduling block are uploaded to the data archive (but not yet released) and passed through the ASKAP continuum validation package^a using default parameters. This package takes the final image, noise map, and Selavy catalogue as input and produces metrics and data quality flags based on a number of validation tests^b. The following metrics are used for each of these tests using ASKAP data only:

- Fraction of sources considered resolved, given by the difference in the integrated (S_{int}) and peak (S_{peak}) flux densities, and local noise σ . We consider a source to be resolved when $(S_{\text{int}} - S_{\text{peak}}) / \sqrt{dS_{\text{int}}^2 + dS_{\text{peak}}^2 + \sigma^2} > 3$, where dS_{int} and dS_{peak} are the estimated measurement errors in S_{int} and S_{peak}
- Reduced χ^2 of differential Euclidean source counts
- Median RMS value (from Selavy noise map)
- Median in-band spectral index (from Selavy catalogue, measured from Taylor term images)

The following additional metrics are used with respect to selected point sources, cross-matched to the reference catalogue that provided the most matches, which for the pilot, is SUMSS

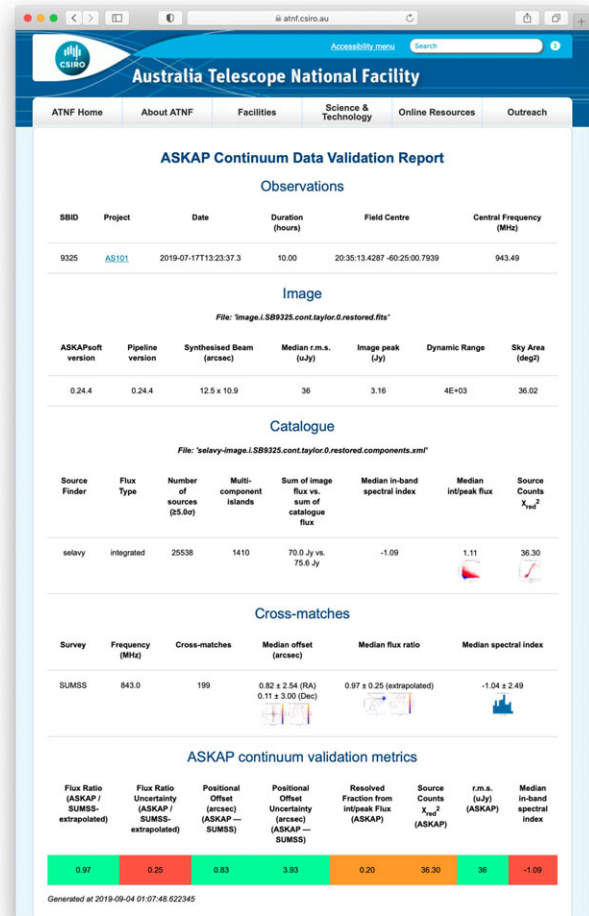


Figure 8. An example validation report for one of the processing runs for SB9325, including the metrics and their flags. A higher-resolution version is available online².

(Mauch et al. 2003), which has a resolution of ~ 45 arcsec at an observing frequency of 843 MHz:

- Median absolute deviation (MAD) of the ratio of the flux density of the reference catalogue to the ASKAP flux density, after correcting for the frequency difference assuming $\alpha = -0.8$,
- Flux density ratio uncertainty, calculated from the MAD
- Positional offset, given by the median compared to reference catalogue
- Positional offset uncertainty, calculated from the MAD

An example report^c for one of the processing runs for SB9325 is shown in Figure 8, including a summary of the metrics and their flags. Each metric is flagged as good, bad, or uncertain based on selected tolerance values^d. The metrics and flags are associated and archived with the data, and the validation reports are automatically uploaded as a report under project AS101^e.

^cReports are available from https://www.atnf.csiro.au/research/ASKAP/ASKAP-validation/commissioning/AS101/SB9325/validation_image.i.SB9325.cont.taylor.0.restored_askapops_2019-09-03-101300/

^dThe metrics are described in detail in <https://confluence.csiro.au/display/askapst/Continuum+validation+metrics>

^e<https://www.atnf.csiro.au/research/ASKAP/ASKAP-validation/commissioning/AS101/>

^a<https://confluence.csiro.au/display/askapst/Continuum+Validation>

^b<https://confluence.csiro.au/display/askapst/Continuum+validation+metrics>

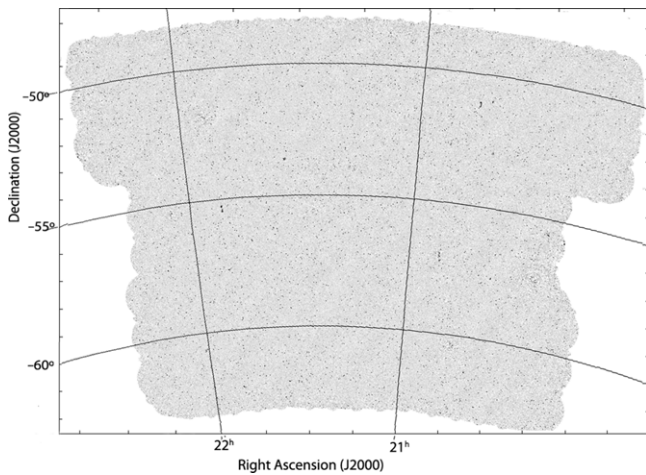


Figure 9. The resulting native resolution ($13'' \times 11''$) image of the 270 deg^2 EMU Pilot Survey, containing about 220 000 radio sources. The rms noise level is $25\text{--}30 \mu\text{Jy beam}^{-1}$, and the peak flux density is $3.14 \text{ Jy beam}^{-1}$.

The final validation process is done by members of the EMU team and includes

- inspecting each of the validation reports described above,
- inspecting the images to search for artefacts,
- examining quantities such as the variation of restoring beam among the 36 beams used in the mosaic.

Data deemed to be acceptable are then released to the public domain on the data archive, described in Section 5.1. If the data are not found to be acceptable, then the data are removed from the archive and we request a re-observation.

4. Value-added processing

To mitigate some of the data issues in the initial public data release and to produce a unified image and source catalogue covering the full EMU-PS field, we conduct value-added processing on the initial public data release to generate a value-added data release. This value-added processing also includes some optical and infrared ancillary data, as described below.

4.1. Merging tiles

The initial public release of the survey data consists of 10 overlapping tiles, each with its own source catalogue. Simply merging these catalogues generates a large number of duplicate sources, which must be reconciled to maximise the information integrity and consistency. This approach also fails to take full advantage of the additional information, such as increased sensitivity, available where tiles overlap.

To overcome these issues, we merged the 10 tiles in the image plane using the ASKAPsoft task *linmos*, which performs a weighted average of the data in overlapping regions. The merged data set is shown in Figure 9. We refer to this image, which has a typical spatial resolution of 11–13 arcsec, as the ‘native resolution image’.

4.2. Convolution to a common restoring beam size

A problem with the native resolution image is that the point spread function (psf) varies from beam to beam over the field, so that

both the flux density scale and also the spectral indices vary from beam to beam. To overcome this problem, we created a version of the data in which each PAF beam is individually convolved with a Gaussian kernel to obtain a common circular restoring beam of 18 arcsec FWHM. We then recombined all beams into a weighted average using the ASKAPsoft task *linmos*. We refer to this data set as the ‘convolved image’.

We then ran the *Selavy* source finder on the convolved image, to produce a catalogue of components and islands. This convolved catalogue has 220 102 components. These ‘convolved’ data are recommended over the ‘native’ data product for the measurements of flux density and spectral index. However, the data products in native resolution are still optimum for studies of morphology, or when the higher resolution is needed.

4.3. Separation of sources into simple and complex

Many value-added operations, such as measuring spectral index, and cross-identifying to optical/IR catalogues, are far more complex for extended or complex sources than for simple, compact sources. These techniques are still under development for the full EMU survey.

We therefore divided the source catalogue into ‘simple’ and ‘complex’ sources. A sophisticated technique for this separation is still under development, so for the purposes of this paper we used a simple technique in which we defined islands with only one component (specifically, with *has_siblings* > 0) to be simple, and all other islands are defined to be ‘complex’. This technique results in a catalogue of 178 921 components, so that about 81% of sources in the catalogue are ‘simple’.

Many ‘complex’ sources are classical FRI or FRII sources (Fanaroff & Riley 1974), but our high sensitivity to low surface brightness has also enabled the detection of several peculiar-looking sources that are quite unlike those seen in earlier surveys such as NVSS (Condon et al. 1998) or FIRST (White et al. 1997). In Section 6, we discuss a small sample of these peculiar objects, which will be further explored in subsequent papers.

We expect about half of the ‘simple’ sources to be star-forming galaxies (SFGs), with the remaining half to be AGN. It is this simple sample for which we obtain multiwavelength data in this paper. The rest of the value-added processing described here is concerned only with this simple catalogue, and the value-added processing of the complex sources will be described in a future paper (Marvil et al., in preparation).

In Table 6, we list the numbers of sources remaining at each stage of the value-added processing.

4.4. Spectral indices

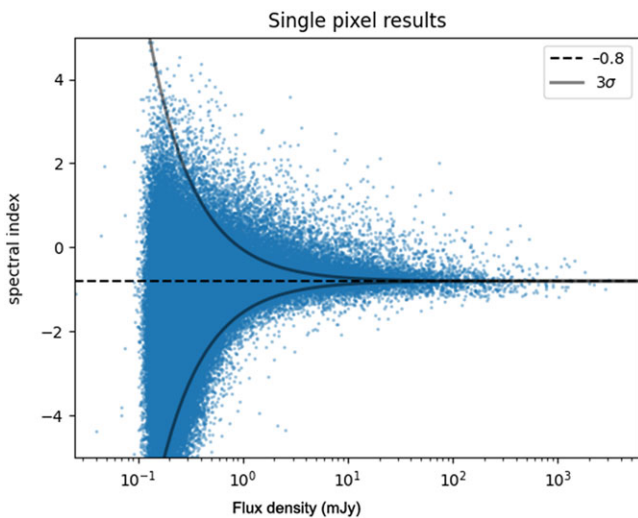
Spectral indices of the simple sources are measured over the 288-MHz bandwidth of ASKAP using the Taylor term technique described above. We measure spectral indices by calculating them from the Taylor terms at the peak pixel of each component, in the convolved data set. Note, as discussed above, that this procedure differs from that in the initial public data release, which we consider to be unreliable.

We also explored using the third Taylor term, which would measure spectral curvature, but found that very few sources had a measurable spectral curvature in the 288-MHz bandwidth of these observations. More importantly, we found that introducing a third Taylor term increased the uncertainty in the first two Taylor terms without increasing the accuracy, presumably because we are

Table 6. Numbers of sources remaining after each stage of the value-added processing.

| Criterion | # sources | Percentage of simple source sample |
|-------------------------------------|-----------|------------------------------------|
| Initial source extraction | 220 102 | n/a |
| Restrict to simple sources | 178 921 | 100 |
| CATWISE2020 Crossmatch* (10 arcsec) | 170 703 | 95 |
| CATWISE2020 Crossmatch (3 arcsec) | 134 657 | 75 |
| DES DR1 Crossmatch (2 arcsec) | 107 735 | 60 |
| DES DR1 Crossmatch* (1 arcsec) | 91 811 | 51 |
| Photometric redshift | 81 938 | 46 |

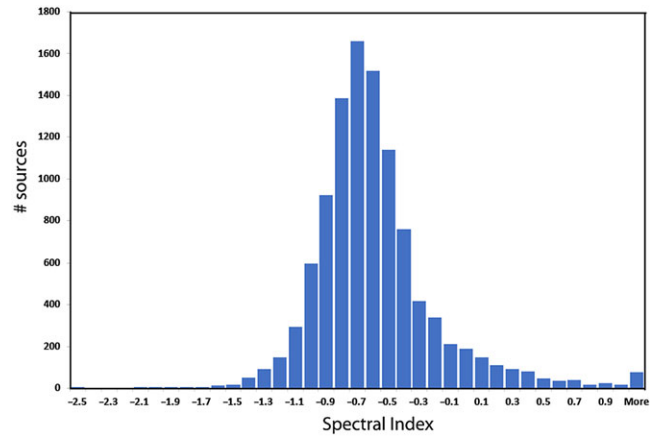
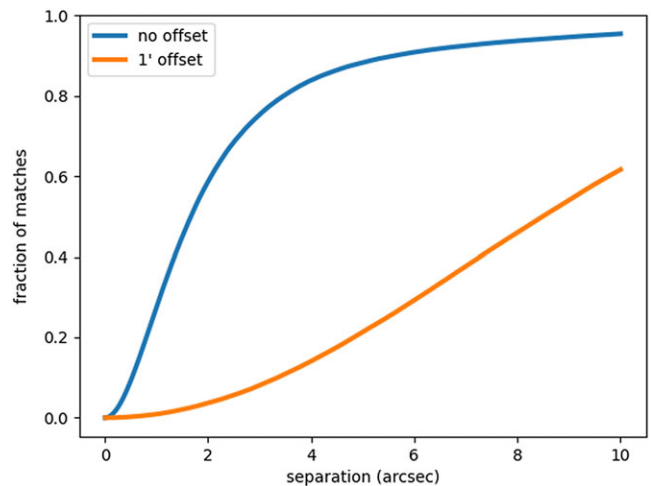
Asterisked rows are shown for information but are not used in the subsequent selection step. Photometric redshifts are taken from Zou *et al.* (2019), Zou *et al.* (2020), and Bilicki *et al.* (2016).

**Figure 10.** The measured spectral index as a function of flux density. The two solid lines show the 3σ uncertainty for a source of spectral index -0.8 . Note the excess of sources with a positive spectral index, discussed in Section 6.9.

introducing a third free parameter which is primarily driven by noise.

The distribution of the resulting spectral indices as a function of flux density is shown in Figure 10. Based on the noise measured in the TT1 image, the 1σ spectral index uncertainty of a source with flux density S mJy is $0.25/S$. The spectral index of a 2.5-mJy source, therefore, has a standard error of ~ 0.1 , and spectral indices of sources weaker than this will be increasingly uncertain.

A histogram of the spectral indices for the 10458 sources with flux density > 2.5 mJy is shown in Figure 11. The peak is at a spectral index of -0.7 , as expected for surveys of mJy radio sources, with a tail of steeper spectrum sources extending to $\alpha < -1.3$. Such ‘ultra-steep spectrum sources’ are well known in the literature (e.g. Afonso *et al.* 2011) and can be an indicator of high redshift sources. There is also an unexpected tail of sources with positive spectral indices. Such sources are also well known (e.g. Healey *et al.* 2007) but are relatively rare. Here, however, they appear to constitute a significant fraction of EMU-PS sources. This is discussed further in Section 6.9.

**Figure 11.** A histogram of measured spectral index as a function of flux density, for the 10458 sources with flux density > 2.5 mJy.**Figure 12.** The fraction of simple radio sources (as listed in Table 6) matched with a CWISE source as a function of separation, both for unshifted data and for data shifted by one arcmin.

4.5. Multi-wavelength cross-identifications and redshifts

For cross-identifying simple sources, we use a simple nearest-neighbour cross-identification algorithm and show below that this gives an acceptable completeness and false-ID rate. Norris *et al.* (2006) found that cross-matching with $3.6\text{-}\mu\text{m}$ *Spitzer* infrared data and then cross-matching the infrared with optical gave a lower false-ID rate than matching radio with optical directly. We therefore adopt this procedure here, and first match the radio against the W1 band ($3.4\ \mu\text{m}$) of the CATWISE2020 catalogue (Marocco *et al.* 2021), hereafter referred to as ‘CWISE’, and then cross-match the CWISE positions against the DES DR1 optical catalogue (Abbott *et al.* 2018).

We measured the number of cross-matches between the radio and the infrared as a function of separation, and then estimated the false-ID rate by shifting the radio positions by 1 arcmin and then repeating the cross-match. The result is shown in Figure 12. The choice of an optimum search radius depends on the application (i.e., whether the goal depends on maximising the number of cross-matches or minimising the number of false-IDs). In producing the cross-matched catalogue, we include all cross-matches

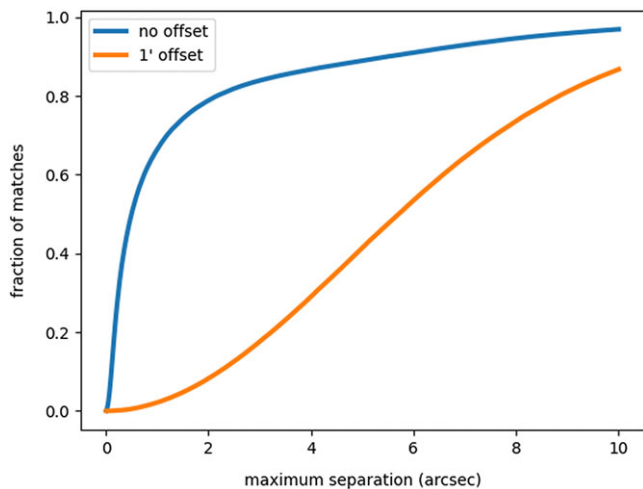


Figure 13. The fraction of radio sources with a CWISE position matched with a DES DR1 source as a function of separation, both for unshifted data and for data shifted by one arcmin.

up to a search radius of 10 arcsec so that users can choose their optimum search radius, but for further work herein we limit our analysis to a maximum search radius of 3 arcsec, at which we find an 8% false-ID rate and a 75% total cross-match rate (which includes the false-IDs). The resulting numbers of sources are listed in Table 6.

Because of the high numbers of faint CWISE sources, we also explored the effect of introducing a cut-off in the CWISE flux densities, so only the brighter sources would be cross-matched to radio sources, but found that had a negligible effect on the false-ID rate, while significantly reducing the number of true IDs, and so no cut-off is used.

To cross-match the CWISE IR positions against DES optical positions, we again explored the false-ID rate and the total-ID rate as a function of search radius, and show the results in Figure 13. As a result, we adopt a search radius of 2 arcsec. The resulting numbers of sources are listed in Table 6.

There is no major spectroscopic redshift survey covering the EMU-PS field, but a large number of photometric redshifts are available from Bilicki et al. (2016) (using their ‘main’ catalogue), and from Zou et al. (2019; 2020), and we also include those in the catalogue. Throughout the rest of this paper, redshifts given without a citation refer to these redshifts used in the EMU-PS catalogue.

4.6. Astrometric precision

For each source that was cross-matched with a CWISE catalogue source, we measured the offset in position, as a check on the precision of the positions of the radio components. The result is shown in Figure 14, showing a mean offset of ~ 0.3 arcsec, which is small compared to the 18 arcsec resolution of the convolved data. The positions in the catalogue have not been corrected for this insignificant offset.

4.7. Flux density accuracy

To estimate the flux density accuracy, we select EMU-PS sources stronger than 6 mJy (the minimum flux density for sources in the SUMSS (Mauch et al. 2003) catalogue) and cross-match them

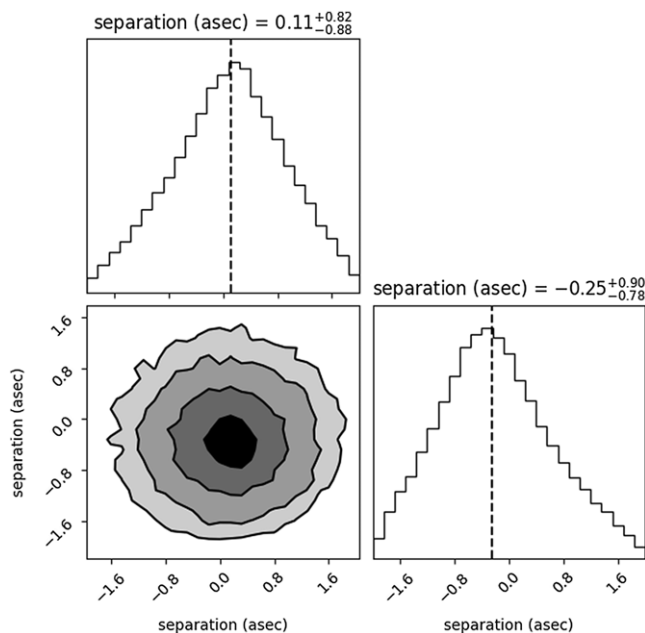


Figure 14. A plot showing the difference in position of radio sources compared to the matching CWISE source in the W1 band, showing a mean offset of ~ 0.3 arcsec, which is small compared to the 18 arcsec resolution of the convolved data. The horizontal axis is Right Ascension and the vertical axis is Declination.

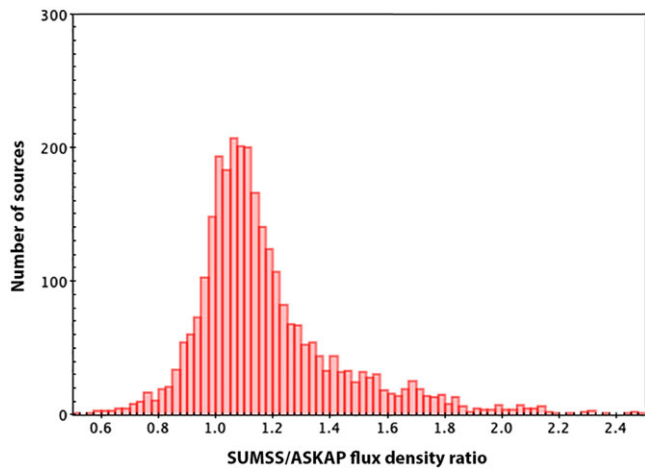


Figure 15. The ratio of peak flux densities between EMU-PS and SUMSS for simple sources with EMU-PS flux densities > 6 mJy, and with catalogued positions within 3 arcsec.

to SUMSS sources using a 3-arcsec search radius, which selects about 50% of the SUMSS sources, and tends to exclude the very extended SUMSS sources. We then calculate the ratio of peak fluxes in the EMU-PS and SUMSS catalogues. The result is shown in Figure 15.

Ideally, we would convolve the EMU-PS to the 45-arcsec resolution of SUMSS and then repeat the source extraction, but then it would not be matched to the EMU-PS value-added catalogue. Because we have not done this convolution, some SUMSS peak flux densities are boosted by components which are included in the SUMSS beam but not in the EMU-PS beam. This increases the scatter of the ratios so that the measured scatter in the ratio is an overestimate of the uncertainty in the EMU-PS flux density scale.

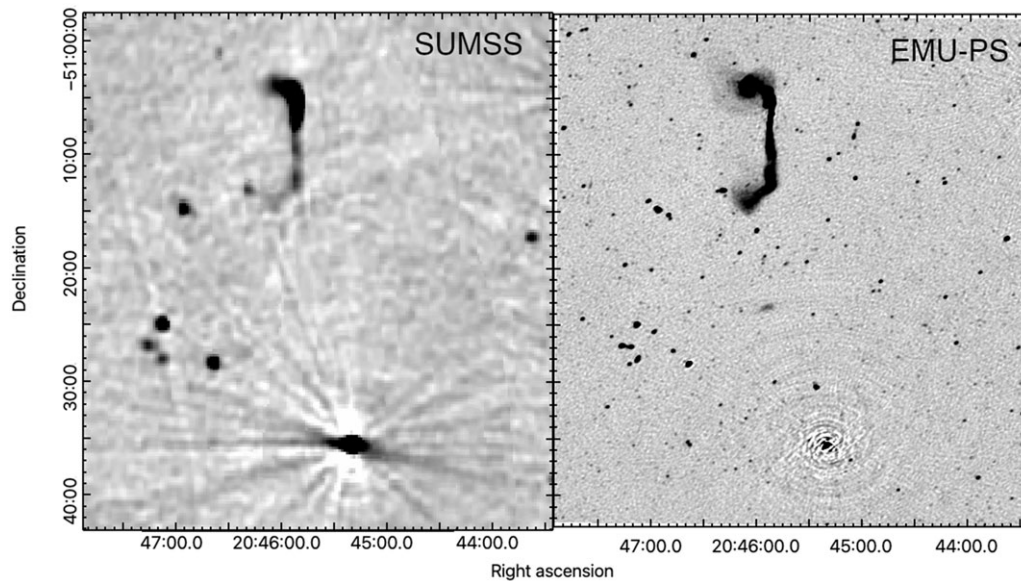


Figure 16. A typical section of the survey field, covering about 0.3 deg^2 (or about one thousandth of the area of the EMU Pilot Survey) which contains about 250 radio sources). On the left is the SUMSS image (Mauch *et al.* 2003) and on the right is the EMU-PS image. Prominent in this image is the Giant Radio Galaxy ESO 234-68. The maximum flux density of ESO 234-68 in the EMU-PS image is $58.8 \text{ mJy beam}^{-1}$, and that of the strong source at the bottom of the image (PMN J2045-5135) is $1.06 \text{ Jy beam}^{-1}$. The rms of the EMU-PS image is $25\text{--}30 \text{ } \mu\text{Jy beam}^{-1}$, and that of the SUMSS image is $\sim 1.25 \text{ mJy beam}^{-1}$.

We note the following features of Figure 15.

- The EMU-PS central frequency of 944-MHz differs from the SUMSS central frequency of 843 MHz, and, assuming a spectral index of -0.8 , we expect the peak of the distribution to occur at a ratio of $\sim (944/843)^{0.8} = 1.09$ as observed.
- The histogram is more extended on the right, presumably because of the larger size of the SUMSS beam which will boost the SUMSS peak flux as discussed above.
- The left of the histogram is approximately Gaussian with a standard deviation of ~ 0.12 .

We therefore estimate our flux density scale uncertainty for strong sources to have a maximum value of $\sigma \sim 12\%$. To this should be added in quadrature the estimated flux density scale standard error for SUMSS of 3% (Mauch *et al.* 2003).

The measured flux density of weaker sources will be degraded by a factor of $1/\text{SNR}$, where SNR is the local signal-to-noise ratio. As we have rejected sources from the EMU-PS catalogue with $\text{SNR} < 5$, this may add an uncertainty of up to 20% (to be added in quadrature) to the quoted flux densities of weak sources.

5. Results

5.1. Data summary and access

The EMU-PS has produced an image of about 270 deg^2 of the radio sky at 944 MHz, with a spatial resolution of $\sim 11\text{--}13 \text{ arcsec}$ and an rms sensitivity of $\sim 25\text{--}30 \text{ } \mu\text{Jy beam}^{-1}$.

A problem with large surveys is that it is difficult to convey the scale and depth of the image in a journal paper. Figure 9 shows the entire native resolution image, and Figure 16 shows a random section of it, which covers about one thousandth of the area of the EMU-PS. An interactive interface to the image of the entire survey field in HiPS format is available on <http://emu-survey.org>.

After observing, processing, and validation by the EMU survey team, the data from each observation are placed on the CSIRO ASKAP Science Data Archive (CASDA) data server and made available to the public as described below. These data consist of all the data from each day's observations, known as a 'tile', including images and tables of extracted components and islands. We call this catalogue the EMU Pilot Initial Public Data Release. The validation metrics and flags are associated with each tile and are fully queryable via table access protocol (TAP).

The data are then processed by merging tiles into a common image covering the whole field of the EMU-PS. The resulting data release of this image is called the 'native' value-added data release.

As described in Section 4, we then smooth the native resolution image to a constant resolution of 18 arcsec, perform source extraction, and separate the resulting catalogue of 220 102 components into simple, single, components (81%), and more complex sources (19%). We also perform cross-identifications of the simple sources with other available multiwavelength products.

We call this science-ready data set the 'Convolved' data set. The resulting image for an area of sky covering an object of interest is shown in Figure 17, which shows the three data products: the initial public data release, the added-value 'native' data release with $11\text{--}13 \text{ arcsec}$ resolution, and the added-value 'convolved' data release with 18 arcsec resolution.

All three data products from the EMU-PS (the initial public data release, the added-value 'native' data release with $11\text{--}13 \text{ arcsec}$ resolution, and the added-value 'convolved' data release with 18 arcsec resolution) are released via the CASDA data server described below. The initial public data release is currently available in the public domain, but the two added-value data releases are available only to EMU members for a proprietary period of 1 year from the date of publication of this paper, after which they will be released into the public domain. However, EMU is an open collaboration, and other astronomers are welcome to join the project,

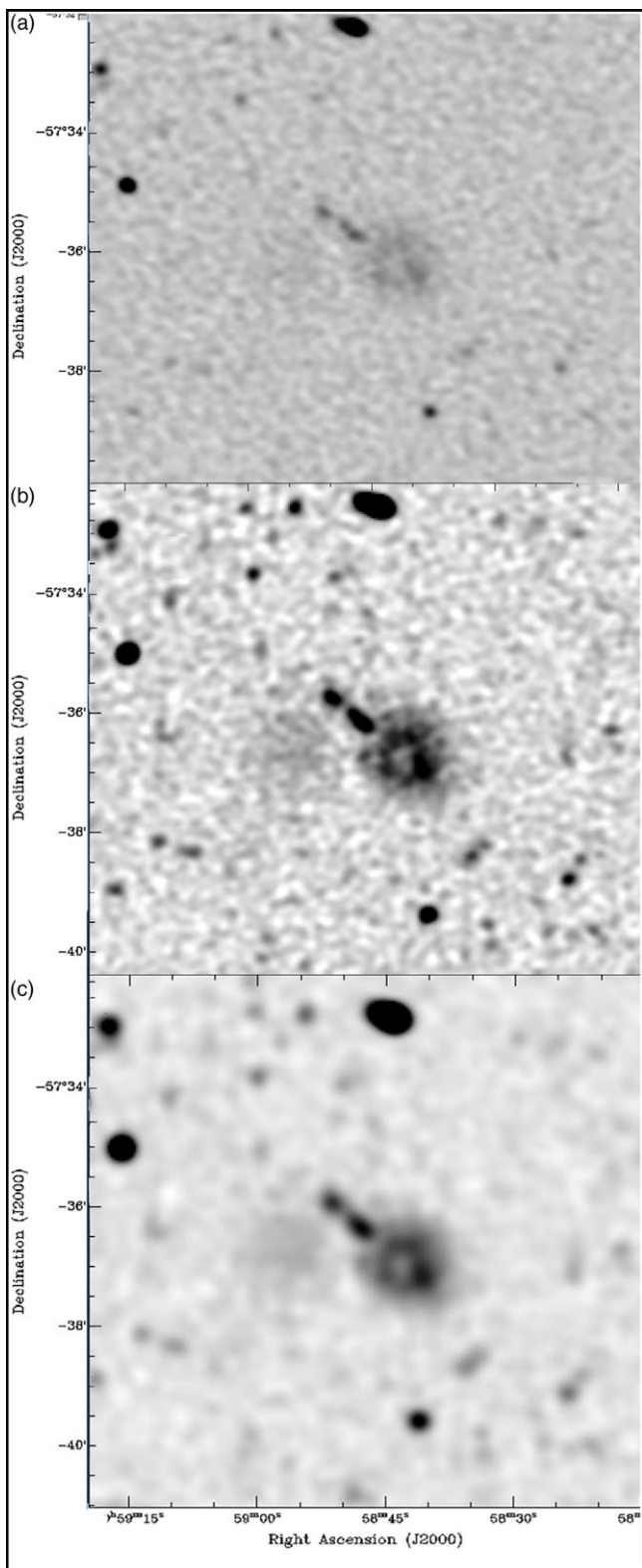


Figure 17. A sample of the final image, showing the three data products on a region, covered by three tiles, containing two of the ‘Odd Radio Circles’ (Norris et al. 2021): (a) the initial public data release from a single tile (SB9351) (resolution 11×13 arcsec, rms = $40 \mu\text{Jy beam}^{-1}$), (b) the added-value ‘native’ data release with 11×13 arcsec resolution, from the merged tiles, rms = $25 \mu\text{Jy beam}^{-1}$, and (c) the added-value ‘convolved’ data release with 18 arcsec resolution, rms = $25 \mu\text{Jy beam}^{-1}$. The peak flux density in this image is $4.6 \text{ mJy beam}^{-1}$.

and access the proprietary data, provided they agree to the EMU data and publication policies.

The EMU-PS initial public release data in the CASDA are open to the public domain. To download data from CASDA, users need to obtain a CASS Online Proposal Applications and Links (OPAL) account^f.

CASDA is described in detail by Chapman et al. (2017) and Huynh et al. (2020). In brief, CASDA is implemented across two data centres, the Pawsey Supercomputing Centre in Perth and the CSIRO data centre in Canberra. So-called ‘backend’ functions such as deposit, storage, and data access are implemented at Pawsey, while the ‘frontend’ functions such as the user interface and authentication are implemented at the CSIRO data centre.

The simplest way to access the data is via the CASDA web user interface. From the CASDA webpage^g, select ‘Access CASDA via the Data Access Portal’, to be taken to the Observation Search user interface. EMU-PS data can be obtained by searching for ‘Released’ data under project code AS101. EMU-PS data have Digital Object Identifiers (DOIs) which provide a persistent resolvable link to the data. Table 7 gives the DOI for each data product discussed in this paper. The DOI links to the collection page; from there click on ‘files’ and select the files to download.

CASDA also implements several Virtual Observatory services to maximise the usability and interoperability of ASKAP data products and allow for automated scripted access. For example, the TAP can be used to search for EMU-PS observations under project code AS101, using an application such as TOPCAT (Taylor 2005) or Aladin (Boch & Fernique 2014; Bonnarel et al. 2000). A CASDA module has recently been added to the Python `astroquery`^h package. Using this Python API, the EMU-PS images can be accessed and downloaded with a cone search of the EMU-PS pointings.

All public data (tables and images, and u, v data) are available from CASDA (see Table 7) and a listing of all ASKAP observations is on the Observation Management Portal (OMP)ⁱ. OMP allows the user to select observations by several parameters including date, SBID (listed in Table 3), or project name (AS101 for EMU).

5.2. Sensitivity to compact sources

The EMU-PS survey reaches a typical sensitivity of $25\text{--}30 \mu\text{Jy beam}^{-1}$ rms. This is about a factor of two above the calculated thermal noise sensitivity ($\sim 13 \mu\text{Jy beam}^{-1}$), which we tentatively attribute to the following causes.

- Timing errors in the correlator cause a significant fraction of data (30–50%) to be flagged, resulting in a loss of data. Work is in progress to identify and eliminate the cause of this problem.
- The data calibration processes are in a preliminary state. By the time of the final EMU survey, we expect to have developed a sky model which will be used to calibrate the data and remove strong sources prior to cleaning.
- A dynamic range problem, which is currently being addressed, causes diffraction patterns around strong sources.

^f<https://opal.atnf.csiro.au/>

^g<https://casda.csiro.au>

^h<https://astroquery.readthedocs.io>

ⁱ<https://apps.atnf.csiro.au/OMP/index.jsp>

Table 7. Available data products, including Digital Object Identifiers (DOIs) that can be used to access the data described in this paper.

| Description | DOI |
|--|---|
| Initial Public Data Release images | https://doi.org/10.25919/5f27829da27ba |
| Initial Public Data Release catalogues | https://doi.org/10.25919/5f27823fa37e2 |
| Added-value Data Release native resolution image | https://doi.org/10.25919/exq5-t894 |
| Added-value Data Release convolved image (TT0) | https://doi.org/10.25919/exq5-t894 |
| Added-value Data Release convolved image (TT1) | https://doi.org/10.25919/exq5-t894 |
| Added-value Data Release convolved catalogue | https://doi.org/10.25919/exq5-t894 |

Notes:

- The initial public data release is immediately available, but the value-added releases are available only to members of the EMU collaboration for 1 year from the date of publication of this paper, after which they become public.
- All catalogues contain island and component information, and, for the added-value catalogue, cross-identifications and redshifts, where available.
- TT0 and TT1 refer to Taylor Term 0 image (total power) and Taylor Term 1 image (TT0 \times spectral index)

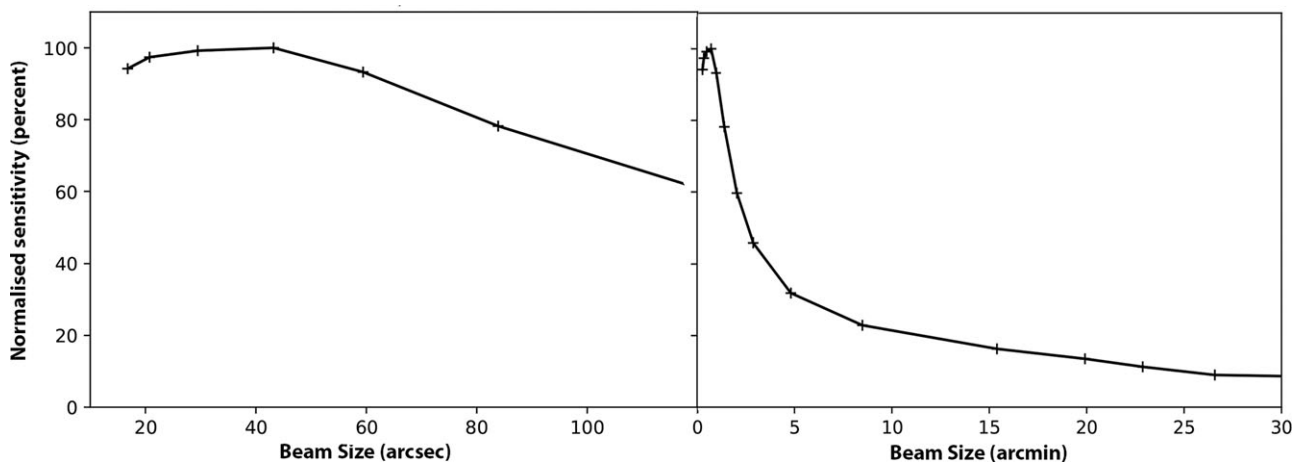


Figure 18. The sensitivity of EMU-PS as a function of spatial scale. The plot was made using visibility data from a single beam and pointing of an interleaved observation (2-h observation, 288-MHz bandwidth, scaled to the EMU-PS observing frequency of 944 MHz) which was filled with Gaussian noise and various uv tapers were applied to shape the beam size. We then measured the image noise (effectively the sensitivity at the scale associated with the uv taper). The two plots show the same result over different ranges of spatial scale.

- The primary beam correction assumes a Gaussian profile across each PAF beam. This is being replaced by a profile based on holographic measurements which will be beam-specific.
- The lack of direction-dependent calibration, which we hope to address in the future.

After correcting these errors, and including a confusion noise of about $9 \mu\text{Jy beam}^{-1}$, we expect the full EMU survey (conducted at a centre frequency of ~ 944 MHz) can potentially reach an rms of about $17.5 \mu\text{Jy beam}^{-1}$.

5.3. Sensitivity to extended emission

As well as its high sensitivity to compact sources, the survey also has high sensitivity to extended low surface brightness emission, because of the large number of short spacings in the ASKAP array.

In Figure 18, we show a plot of the sensitivity of EMU-PS as a function of spatial scale, obtained by running simulated observations with different tapers, producing different beam sizes.

The sensitivity of $25\text{--}30 \mu\text{Jy beam}^{-1}$ at the native resolution of $11\text{--}13$ arcsec is almost unchanged at the convolved resolution of 18 arcsec and continues at a similar level beyond the 45 -arcsec resolution of SUMSS (Mauch *et al.* 2003), which has a median rms

sensitivity of $1.27 \text{mJy beam}^{-1}$. The effect of this high sensitivity to low surface brightness emission is demonstrated in Section 6.

5.4. Source counts and confusion

Figure 19 shows the differential source counts normalised to a non-evolving Euclidean model ($n \propto S^{2.5}$) obtained from the EMU-PS catalogue (black symbols), rescaled from 943.5 MHz to 1.4 GHz by assuming $\alpha = -0.7$. Two counts' determinations are shown: one referring to the *island* catalogue, where components of complex sources are merged together (filled diamonds) and one referring to simple sources only (empty diamonds). The source counts are corrected for both Eddington bias (Eddington 1913; Eddington 1940) and resolution bias (i.e. the incompleteness introduced by the fact that a larger source of a given total flux density will drop below the signal-to-noise threshold of a survey more easily than a smaller source of the same total flux density). This is done following standard recipes in the literature (see e.g. Prandoni *et al.* 2001; 2018; Mandal *et al.* 2021).

Figure 19 shows for comparison some of the widest-area samples available to date at 1.4 GHz. This includes sub-mJy surveys covering $> 1 \text{deg}^2$ regions, like PDF (Hopkins *et al.* 2003), VLA-COSMOS (Bondi *et al.* 2008) and the 6deg^2 Westerbork mosaic

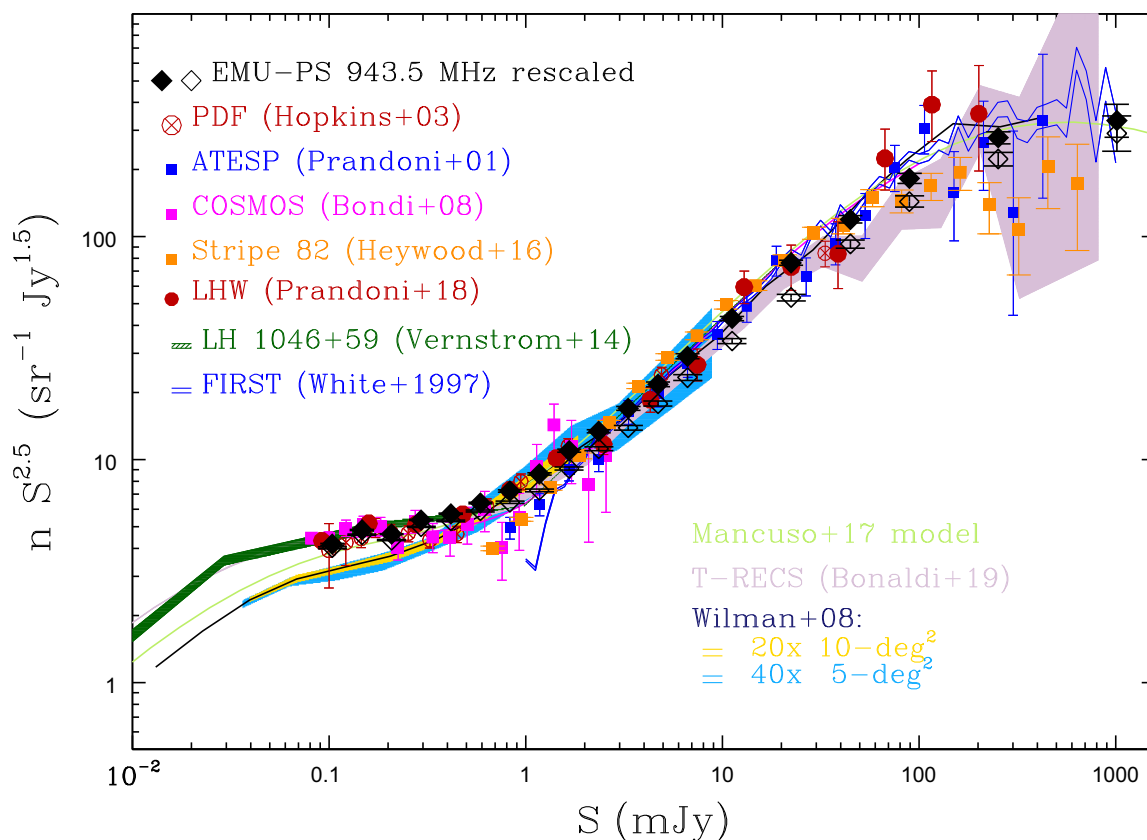


Figure 19. Normalised differential source counts derived from the 270 deg² EMU-PS survey for the *island* catalogue (black filled diamonds) and for simple sources only (black empty diamonds). The counts have been rescaled from 943.5 MHz to 1.4 GHz by assuming $\alpha = -0.7$. Also shown for comparison are the counts derived from 1.4 GHz > degree-scale surveys (symbols and colours as indicated in the figure). Vertical bars represent Poissonian errors on the normalised counts. Systematic errors due to incompleteness corrections and spectral index assumptions are approximately included in the size of the plotted symbols. The result of the $P(D)$ analysis performed by (Vernstrom et al. 2014, rescaled from 3 to 1.4 GHz by assuming $\alpha = -0.7$) is indicated in dark green. The black solid line represents the predicted counts from 200 sq. deg. of the S3-SEX simulations (Wilman et al. 2008). The light blue and yellow shaded areas illustrate the predicted cosmic variance effects for survey coverages of 5 and 10 deg², respectively (obtained by splitting the S3-SEX simulation in 40 5-deg² and 20 10-deg² fields, respectively). The 25 deg² medium tier of the more recent T-RECS simulations (Bonaldi et al. 2019) is represented by the purple shaded area. Finally, the Mancuso et al. (2017) radio source evolutionary model is shown by the light green line.

covering the Lockman Hole region (LHW: Prandoni et al. 2018), as well as shallower (> 1 mJy) but larger ($\gg 10$ sq. degr.) surveys like ATESP (Prandoni et al. 2001), SDSS Stripe 82 (Heywood et al. 2016) and FIRST (White et al. 1997). Also shown are simulated source counts derived by combining evolutionary models of either classical radio loud (RL) AGN or radio source populations dominating the sub-mJy radio sky, namely SFGs and low-luminosity AGN (LLAGN). In particular, we show the 1.4-GHz counts derived from the recent modelling of Mancuso et al. (2017), light green solid line, the T-RECS 25 deg² medium tier simulation (Bonaldi et al. 2019), as well as different realisations obtained from the S3-SEX simulated catalogue (Wilman et al. 2008): 1×200 deg² (black solid line), 20×10 deg² regions (yellow shaded area) and 40×5 deg² regions (light blue shaded area).

Figure 19 clearly shows that the source counts derived from the EMU-PS *island* catalogue nicely match previous counts and are in good agreement with the most recent models/simulations (Mancuso et al. 2017; Bonaldi et al. 2019). Even more interestingly they provide very robust statistics all the way from ~ 0.1 mJy to > 1 Jy, something which could only be achieved in the past by combining deeper (but smaller) surveys with larger (but shallower) surveys. Finally, it is interesting to note that the counts

derived from simple sources only (black empty diamonds) fall well below the full counts (black filled diamonds) at bright fluxes. This is not surprising as we expect a large contribution from multi-component RL AGN at flux densities $\gg 1$ mJy. On the other hand, no significant difference is observed at sub-mJy fluxes, confirming that this flux regime is dominated by SFG and LLAGN.

5.4.1. Source Confusion

We estimate the source confusion noise, and instrumental noise using the probability of deflection, or $P(D)$ technique (Scheuer 1957). The $P(D)$ distribution of an image is the distribution of pixel intensities (Jy beam⁻¹) which depends on the underlying source count, shape of the beam, and the instrumental noise (see Vernstrom et al. 2014, for a detailed description of the method).

The $P(D)$ method assumes a Gaussian distribution for the instrumental noise and can therefore be affected by imaging artefacts, such as those found around bright sources. We computed the histogram of pixel intensities for the pilot survey image by selecting regions of pixels devoid of any image artefacts, as well as any complex diffuse or extended emission. Rather than a full source count fitting analysis, which is beyond the scope of this paper, we take the deep $P(D)$ source counts derived in Vernstrom

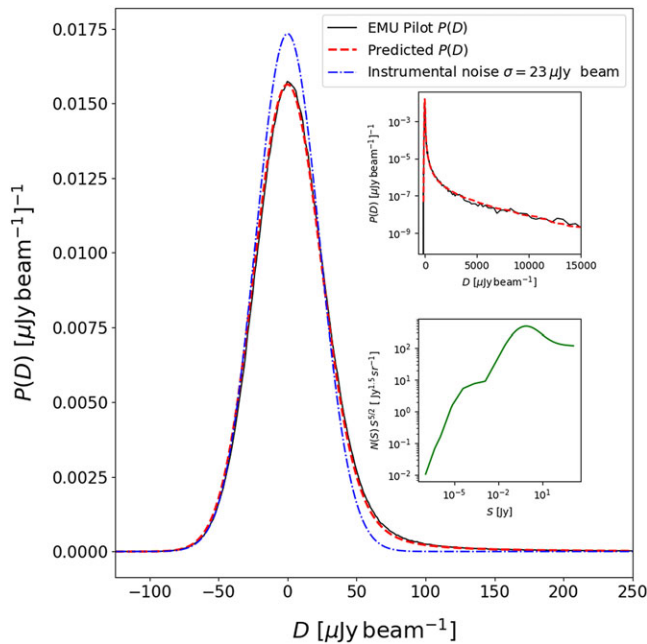


Figure 20. The EMU-PS preliminary $P(D)$ distributions. The solid black line is the probability distribution made from sections of the pilot away from bright sources. The upper right inset shows bright flux density tail of the $P(D)$ distributions. The blue dot-dashed line shows a Gaussian noise distribution of $\sigma = 23 \mu\text{Jy beam}^{-1}$. The red dashed line shows the predicted or model $P(D)$ generated from the source count shown in the lower right inset.

et al. (2014) and scale it to a frequency of 944 MHz using $\alpha = -0.7$. We take the average beam sizes from the individual beams and find $B_{\text{maj}} = 12$ arcsec and $B_{\text{min}} = 10$ arcsec, while using an image of the ‘dirty’ synthesised beam for sources below the clean limit (approximated at $S_{\text{clean}} = 200 \mu\text{Jy beam}^{-1}$). We use an average instrumental noise value of $\sigma = 23 \mu\text{Jy beam}^{-1}$. The image $P(D)$, noise distribution, and model $P(D)$ can be seen in Figure 20.

Without any additional fitting or changes to the parameters or source count, we find very good agreement between the image and model $P(D)$ distributions. The noise-free model $P(D)$ provides an estimate of the confusion noise in the field of $\sigma_{\text{conf}} = 5 \mu\text{Jy beam}^{-1}$. This quick test shows through independent means that the instrumental noise estimate of 20 to 25 $\mu\text{Jy beam}^{-1}$ is accurate. Furthermore, the fact that the scaled source count model provides a good match to the image is a confirmation of accurate source flux densities in the pilot data, and that confusion noise is not a significant factor for our scientific investigations, even when considering the dirty beam sidelobe confusion noise. At the same time, the observations of $P(D)$ are sensitive enough to probe far below the source populations that we can directly detect.

6. Preliminary science results

6.1. Peculiar radio sources

Many unusual radio sources are found in the EMU-PS.

The source PKS 2130-538, shown in Figure 21, has been previously identified as a complex source (e.g. Ekers 1970; Schilizzi & McAdam 1975; Jones & McAdam 1992), and as two radio galaxies (G4Jy 1704 and G4Jy 1705) in the G4Jy Sample (White *et al.* 2020b; White *et al.* 2020a). However, no previous image shows the wealth of detail and low surface brightness emission seen in Figure 21. It

consists of the radio lobes of two host galaxies, one of which (‘Host 1’: 2MASX J21341775-5338101) is the bright galaxy at the centre of the curved northern radio bridge, at a redshift of 0.0781. This is the brightest galaxy of the cluster Abell 3785. The other host galaxy (‘Host 2’: 2MASX J21340666-5334186) is the bright galaxy near the southeast end, at a redshift of 0.0763.

The spectral index image helps to isolate the contributions from these two hosts. In the north, there is a very flat spectrum region ($\alpha \sim 0$) at the position of Host 1, connecting to relatively flat $\alpha \sim -0.4$ – -0.5 jets (‘1’). These then connect to the large bright regions of $\alpha \sim -0.6$ – -0.7 , steepening sharply down the tails to the south to at least -1.5 , beyond which the spectra become more uncertain. All of this is consistent with the behaviour of bent-tail galaxies. In the eastern half, there is a dramatic change in spectral index at the position of the emission associated with the second host; it has its own flat core and steeper lobe/tail structures. Although the overall emission comes from two distinct hosts, it is unclear whether there is an interaction between them, or merely a superposition. An additional curiosity is the thin stream of emission ‘3’ extending eastward from the NE bright region; it has a median spectral index of -2.1 , and both its dynamical origins and particle history do not fit naturally into existing radio galaxy models.

The source PMN J2041-5256, shown in Figure 22, is a double-lobed radio AGN, associated with the host galaxy WISEA J204112.05-525737.7 at a redshift of $z = 0.048$. Previous radio data (Mauch *et al.* 2003; Gregory *et al.* 1994) show only an indistinct extended source corresponding to the nucleus. Its jets (shown with numbers in the figure to indicate their putative host) are presumably being bent by intracluster winds, but the morphology is much more complex than normal bent-tail galaxies. The eastern jet (‘2’) is bifurcated, while the western jet (‘1’) breaks down into a number of blobs, accompanied by a large diffuse area of emission to the west of the source. One possibility is that its relative motion with respect to the intracluster medium (ICM) has a large component along the line of sight; the bifurcated tail and western diffuse extensions would then be more typical of structures seen in bent-tail galaxies, but seen here in projection. If the direction of motion were ~ 20 degrees from the line of sight, the entire source length would be ~ 750 kpc, among the larger bent-tail sources.

Figure 23 shows two diffuse clouds of radio emission whose origin is unclear. The most likely hypothesis is that they represent the remnants of a classical double-lobed radio galaxy in which the central engine has switched off, leaving a remnant radio galaxy. We refer to this object as the ‘Smoking Gun.’

A tentative identification of the host (marked A in Figure 23) is the galaxy WISEA J204837.65-491115.2, at a redshift of 0.10 (Bilicki *et al.* 2016) and which is detected as a $260 \mu\text{Jy}$ unresolved source in the ASKAP image. At that redshift, the largest angular size across the lobes is 530 kpc, which is not unusual for double-lobed radio galaxies. An alternative identification (marked B in Figure 23) of the host is an isolated unresolved $200 \mu\text{Jy}$ radio source which appears to be coincident with the galaxy DES J204835.43-491137.5, at $z = 0.937$ (Zhou *et al.* 2021). If the ‘Smoking Gun’ were actually at this redshift, then the source’s large inferred radio size (2.25 Mpc) would make it a member of the rare class of ‘Giant Radio Galaxies’ (see Section 6.4) and it would also be very luminous ($\sim 4 \times 10^{23}$ W/Hz). This seems unlikely for a fading remnant, and so we think A, at a redshift of 0.1, is more likely to be the host galaxy. We note that the northern lobe is unusually circular and resembles the Odd Radio Circles (ORCs)

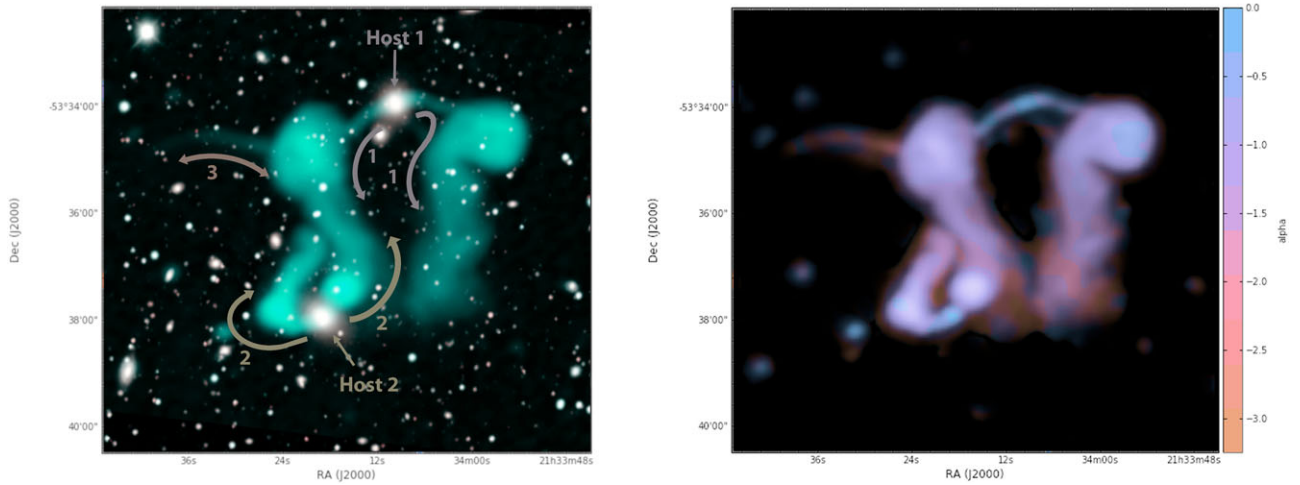


Figure 21. A peculiar radio source found in the EMU Pilot Survey, consisting of a group of distorted radio components, collectively known as PKS 2130–538, and nicknamed ‘the dancing ghosts’. The two host galaxies ($z \sim 0.077$) are seen at the centre of the narrow jets (shown with numbers in the figure to indicate their putative host) which expand into diffuse lobes, probably bent by interactions. On the left is the total intensity greyscale image (shown in turquoise), superimposed on a background of the DES optical image, assembled from the r, g, and i images. On the right is the total intensity image of PKS 2130–538, colour-coded by spectral index. The unconventional colour scheme was constructed using sequential colours on the ‘colour wheel’ (e.g. Itten 1970). The colours were fixed in luminosity, that is, fixed to be constant in luminosity-chroma-hue colour space (Ferrand 2019). In this way, the brightness level on the image represents only the total intensity values. The colour bar indicates the spectral index at a single fixed intensity. Since the spectral index map in this colour scheme was multiplied by the total intensity map, darker versions of colours are associated with fainter regions in the data. The peak flux density in this image is $103 \text{ mJy beam}^{-1}$.

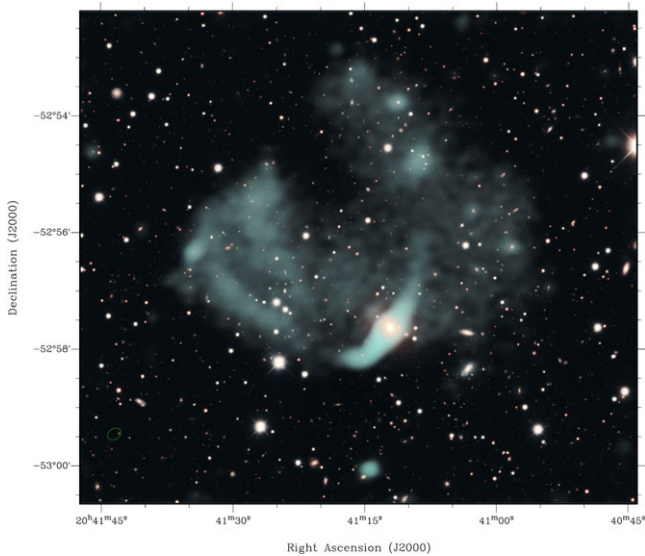


Figure 22. Another peculiar radio source found in the EMU Pilot Survey: a double-lobed radio AGN, known as PMN J2041–5256, with a curious ‘double’ bent tail. The radio data from EMU-PS has been ‘stretched’ to show the faint emission, and then coloured turquoise, and adjusted to emphasise the double tail. DES g-, r-, and i-band data are combined to form the background, which is combined with the radio data using a layer mask in GIMP. Embedded in the tails are several radio sources that may be unrelated to the tailed galaxy. The peak flux density in this image is $58.3 \text{ mJy beam}^{-1}$.

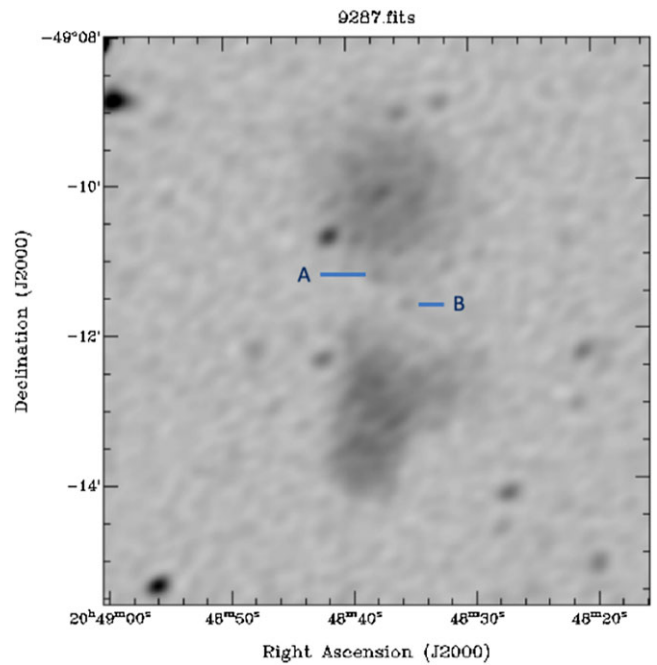


Figure 23. The ‘Smoking Gun’ Galaxy EMU PS J204835.0–491137 consists of the two diffuse radio clouds seen in this image. These are presumably the remnants of a classical double-lobed radio galaxy in which the central engine has switched off. The labels A and B indicate two possible host galaxies, discussed in the text. The peak flux density in this image is $0.87 \text{ mJy beam}^{-1}$.

shown in Figure 17, except that the ORCs don’t show a continuous rise of their surface brightness towards their centres.

Such remnant radio galaxies have previously been reported (e.g. Brienza et al. 2017; Mahatma et al. 2018; Saripalli et al. 2012), but these new observations probe a lower level of surface brightness than earlier studies. Another remnant radio galaxy imaged by ASKAP has also been recently reported (Quici et al. 2021).

However, none of the previously reported remnant radio galaxies has a circular lobe resembling that in Figure 23.

Figure 24 shows the radio source EMU PS J210700.0–501128 (also detected as SUMSS J210704–501206). It appears similar in some ways to PKS 2130–538 shown above (Figure 21) with two bright patches and diffuse tails, presumably blown to the east by

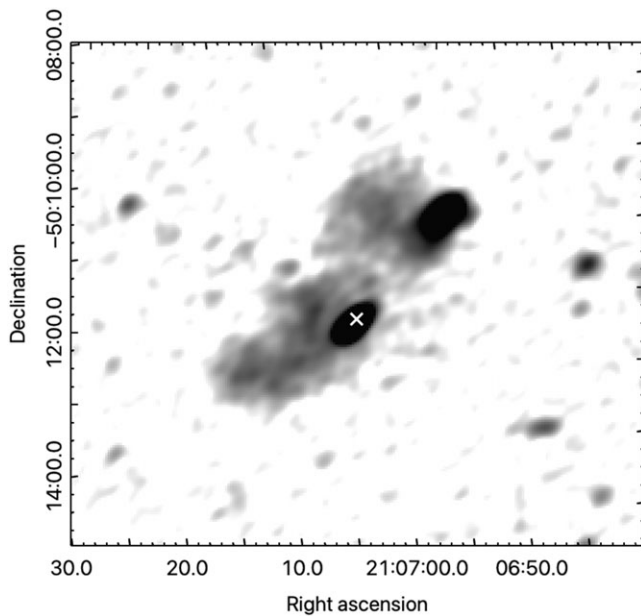


Figure 24. EMU PS J210700.0–501128.8 is an ambiguous case, appearing at first to be a double-lobed source with material blown to the east. But with no host between the bright patches, and the southern bright component coincident with a quasar, marked with an ‘X’, these may be two independent sources with serendipitously similar appearances. The peak flux density in this image is $11.6 \text{ mJy beam}^{-1}$.

relative motion through an external medium. However, there is no obvious host galaxy between the lobes, only a scattering of faint DES galaxies. Instead, the bright southern lobe is coincident with the quasar WISEA J210703.75–501207.7 at a redshift of 0.197 (Monroe *et al.* 2016), also detected in the Second ROSAT all-sky survey (Boller *et al.* 2016). This raises the possibility that the two ‘lobes’ are two independent tailed radio galaxies with very similar morphologies. An apparent overdensity of galaxies visible in both DES and WISE is embedded in the faint southern emission. However, there is no cataloged cluster near this location, and we found photometric redshifts (Zou *et al.* 2019) for only three galaxies within the source confines that would be consistent with the quasar redshift, so there is no evidence for a cluster.

6.2. Odd radio circles

It has been predicted that, because EMU would observe a previously inaccessible part of observational parameter space, it would probably make unexpected discoveries (Norris 2017b). Nevertheless, we were surprised to find an apparently new class of object appearing in the EMU-PS, consisting of circles of radio emission, typically one arcmin across, with no optical or infrared counterpart (Norris *et al.* 2021). The first of these ORCs to be identified is shown in Figure 25, and another example is shown in Figure 17. We do not yet understand the nature of these objects, nor whether they are a single class of object or multiple classes. Since discovering them in EMU-PS, we have subsequently observed them with several other telescopes to confirm their reality and have been able to rule out some potential explanations such as supernova remnants or starburst rings. We have also found more examples in other ASKAP fields (e.g. Koribalski *et al.* 2021). Several ORCs have a galaxy at the centre, typically at a redshift of ~ 0.3 in the currently known examples. Potential explanations are that these central galaxies may be the origins of spherical shock

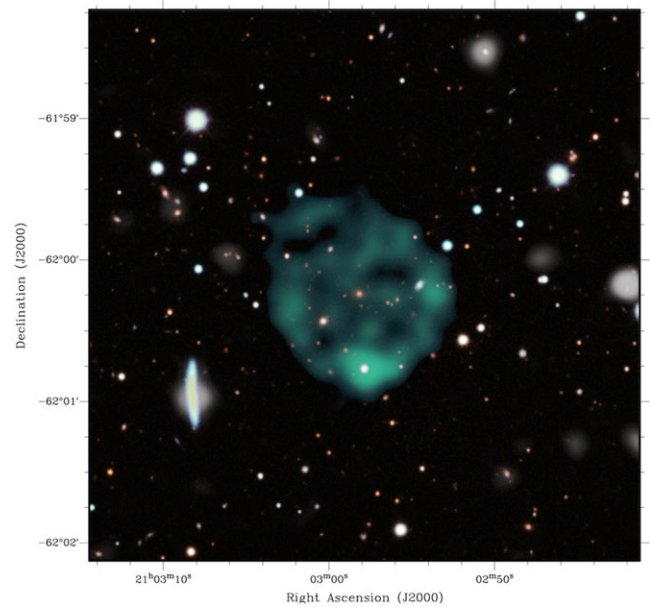


Figure 25. An image of the first ‘Odd Radio Circle’, or ORC, found in EMU-PS (Norris *et al.* 2021). It has no optical counterpart to the diffuse ring, or to other diffuse structure, but has a galaxy at its centre which may be the origin of the ring. The image is based on EMU-PS data at native resolution but enhanced to show faint features as described in Norris *et al.* (2021), particularly the internal structure or ‘spokes’ of the ORC. Radio data are shown in green, and DES optical data are shown in turquoise, magenta, yellow and red, and mainly appear in this image as white.

waves which we see in projection as a ring, or else that we are seeing end-on radio lobes.

6.3. Nearby galaxies

The design of ASKAP was largely driven by its two largest survey science projects: the EMU continuum survey (Norris *et al.* 2011) and the WALLABY spectral line survey (Koribalski *et al.* 2020) with the latter aiming to map neutral hydrogen (H I) over the entire extragalactic sky in the declination range from -90° to $+30^\circ$ to a redshift of ~ 0.26 . WALLABY will generate H I image cubes at ~ 30 arcsec resolution and $\sim 1.6 \text{ mJy beam}^{-1}$ per 4 km s^{-1} channel sensitivity and is expected to detect around half a million galaxies with a mean redshift of ~ 0.05 (Koribalski *et al.* 2020).

The relationship between the integrated radio continuum emission of SFGs, unattenuated by interstellar dust, and their star formation rate (SFR) has been extensively studied, (e.g. Condon 1992; Tabatabaei *et al.* 2017; Davies *et al.* 2017), and the broad correlation is well documented, (e.g. Condon *et al.* 2002; Murphy 2009; Murphy *et al.* 2011; Molnár *et al.* 2021). However, the detailed correlations and the underlying mechanisms are still the subject of much debate (e.g. Heesen *et al.* 2014). Furthermore, the relationship between the atomic neutral hydrogen gas content of galaxies (for $z < 0.2$, where individual galaxy detections are feasible) and their SFR requires further investigation (e.g. Wong *et al.* 2016; Bera *et al.* 2019).

Our most extensive knowledge of the southern sky in neutral hydrogen currently comes from the low-resolution H I Parkes All Sky Survey (HIPASS; Barnes *et al.* 2001) which covers the sky from -90° to $+25^\circ$. HIPASS produced a catalogue of ~ 5000 galaxies out to a redshift of $z = 0.04$ (Koribalski *et al.* 2004; Meyer *et al.* 2004). Corresponding 20-cm radio continuum maps (CHIPASS)

were created by Calabretta et al. (2014). ASKAP delivers a 90-fold (for EMU) or 30-fold (for WALLABY) improvement in angular resolution compared to the HIPASS single-dish beam of ~ 15.5 arcmin.

The survey characteristics of EMU and WALLABY imply that we expect nearly all of the ~ 5000 catalogued HIPASS galaxies to be detected by EMU, and to be well resolved by both EMU and WALLABY. Therefore, the combination of EMU radio continuum and WALLABY H I spectral line measurements of nearby galaxies, combined with other multi-wavelength data, offers the opportunity to study the relationships between star formation, radio continuum emission, and H I emission in great detail. Here we start to explore this field using the EMU-PS observations of a small sample of nearby galaxies which have been detected in HIPASS.

Of the 89 catalogued HIPASS sources in the EMU-PS area, 63 are clearly detected by EMU-PS in the radio continuum. We expect most of the remaining HIPASS sources to be detected in the full sensitivity main EMU survey. A selection of these galaxies is shown in Figures 26 and 27. While no WALLABY H I data currently exist for this field, high-resolution ATCA H I images are available for some of the galaxies.

The most interesting galaxy in Figure 26 is the edge-on spiral NGC 7090. Using the ATCA, Heesen et al. (2016; 2018) obtained detailed radio continuum maps, finding a radio halo with polarised emission up to 6 kpc above the disc correlating with extraplanar H α emission. ATCA H I images (Dahlem et al. 2005) reveal an asymmetric, slightly disturbed disc matching the stellar extent. Another galaxy of interest is the nearly face-on spiral NGC 7125 (see Figure 27), which forms an interacting pair with its northern companion NGC 7126, separated by six arcmin (~ 80 kpc). ATCA H I maps (Nordgren et al. 1997) show a large gas envelope encompassing both galaxies. Once detailed H I spectral line and radio continuum maps are available for large numbers of nearby resolved galaxies, the local and global SFRs and efficiencies can be analysed as a function of H I column density and environment (e.g. Koribalski & López-Sánchez 2009; Wong et al. 2016).

6.4. Giant Radio Galaxies

Giant Radio Galaxies (GRGs) were originally defined as Radio Galaxies (RGs) whose projected linear size was greater than 1 Mpc for a Hubble constant of $H_0 = 50 \text{ km s}^{-1} \text{ Mpc}^{-1}$ (e.g. Ishwara-Chandra & Saikia 1999). However, based on the currently accepted value of $H_0 \sim 70 \text{ km s}^{-1} \text{ Mpc}^{-1}$, RGs larger than 0.7 Mpc are now also considered GRGs. In the compilation of GRGs by Kuźmicz et al. (2018), the EMU-PS area contains only a single GRG, namely PKS 2014–558, first mentioned as a GRG by Jones & McAdam (1992) and recently studied in detail by Cotton et al. (2020).

In a recent ASKAP observation covering 30 deg^2 centred on the Abell 3391/3395 galaxy cluster pair, and of comparable depth and angular resolution as the EMU-PS, Brügggen et al. (2021) found the surface density of GRGs $\gtrsim 1 \text{ Mpc}$ to be $\sim 0.8 \text{ deg}^{-2}$, and that of GRGs $\gtrsim 0.7 \text{ Mpc}$ to be at least $\sim 1.7 \text{ deg}^{-2}$, suggesting that the EMU-PS should contain ~ 200 and ~ 460 such GRGs, respectively.

From a preliminary visual inspection of the EMU-PS area, biased towards sources of larger angular size and featuring a radio nucleus, we found ~ 120 GRGs larger than 1 Mpc and a similar number with sizes between 0.7 and 1 Mpc. We visually cross-identified these with the DES images and catalogues (Abbott et al.

2018) and estimated linear sizes based on photometric redshifts (Bilicki et al. 2016; Drlica-Wagner et al. 2018; Zou et al. 2019). The number of GRGs in EMU-PS is likely to increase with a more thorough visual inspection, the results of which will be reported by Andernach et al. (in prep.).

6.4.1. The Giant Radio Galaxy EMU PS J205139.8–570434

The GRG EMU PS J205139.8–570434 (hereafter GRG J2051–5704), shown in Figure 28, is hosted by 2MASX J20513976–5704334 at $z_{sp} = 0.0602$ (Jones et al. 2009) and its radio emission can be traced over a largest angular size ~ 22.1 arcmin and thus a linear projected size of 1.53 Mpc. It has an FRI radio morphology whose jets are oriented roughly north-south, feature several wiggles, and terminate in diffuse lobes at both extremes of the source. The strong ($S_{944} = 2.12 \text{ Jy}$) source 3.1 arcmin due E, surrounded by diffraction rings, is the well-studied galaxy IC 5063 at $z_{sp} = 0.01135$.

The central region of the new GRG can be recognised in the SUMSS (Bock et al. 1999) images and was even detected at mm wavelengths by the South Pole Telescope (Mocanu et al. 2013). However, the full extended structure shown here has not been previously detected, despite extensive imaging of the neighbouring source IC 5063 (Murphy et al. 2010 and references therein), probably because of the brightness sensitivity and dynamic range limitations.

The host galaxy of GRG J2051–5704 is the brightest galaxy of cluster 400d J2051–5704 (aka MCXC J2051.6–5704, Burenin et al. 2007; Piffaretti et al. 2011) at a redshift of 0.0599. The radio morphology is reminiscent of archetypal FRI sources such as 3C 31 and Hydra A, with wiggles consistent with either the presence of jet instabilities due to interaction with the surrounding gas, or jet precession (e.g. Nawaz et al. 2016). While FRI type sources are rare among GRGs larger than 1 Mpc, a recent LOFAR image showed that the GRG 3C 31 also had an extent $> 1 \text{ Mpc}$ (Heesen et al. 2018).

It is likely that more of these very large GRGs will be detected with next-generation radio telescopes such as ASKAP thanks to the combination of good angular resolution necessary to reveal the inner jet structure and identify the host, as well as high sensitivity to the low surface brightness features such as the outer tails or lobes. We note that Turner et al. (2018) showed from simulations that more sensitive, or lower frequency, observations will reveal FRI galaxies to be much larger than previously thought.

6.5. Radio counterparts to 6dF galaxies

EMU and the EMU-PS overlap the 6dF Galaxy Survey (6dFGS; Jones et al. 2004; 2009), a spectroscopic survey of most of the southern sky containing 125 071 galaxy redshifts with a median redshift of 0.053. While a variety of selection criteria were used for 6dFGS, most 6dFGS galaxies are brighter than $K = 12.65$ and have redshifts of $z < 0.15$. In the EMU-PS region, there are 2506 6dFGS galaxies and, as we discuss below, a large fraction of these galaxies are detected by the EMU-PS.

We measured the flux density of each 6dFGS galaxy using the pixel in the radio continuum maps corresponding to each galaxy's position. This will underestimate the total flux density of spatially resolved galaxies, and aperture bias is relevant as the $13'' \times 11''$ EMU-PS beam and $6.7''$ 6dFGS spectroscopic fibre correspond to less than 3.4 kpc and 2.0 kpc, respectively, for galaxies within 60 Mpc of Earth. Despite these limitations,

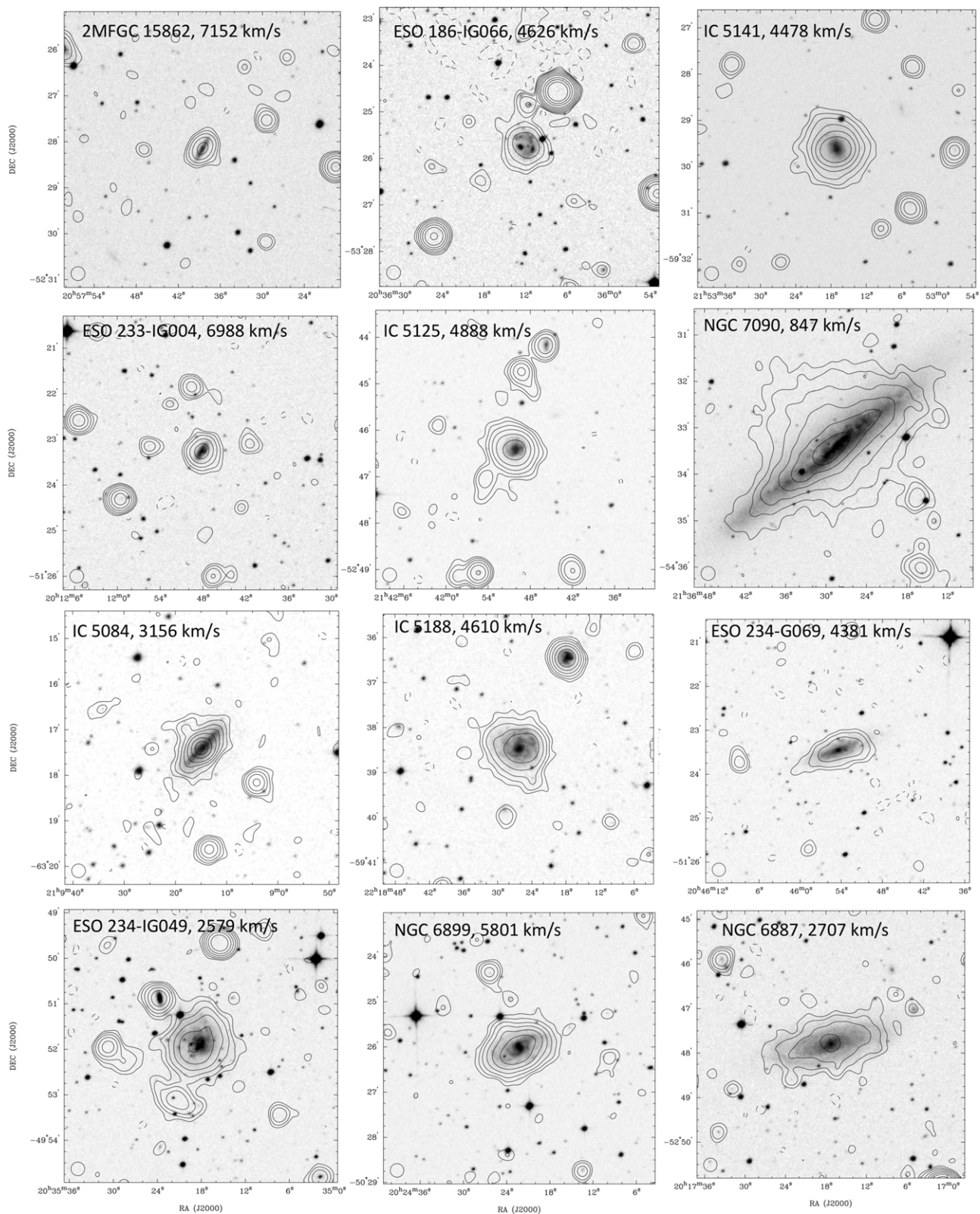


Figure 26. A selection of ASKAP-detected nearby galaxies in the EMU-PS. Optical DSS2 *R*-band images are overlaid with ASKAP radio continuum contours. The contour levels are $-0.09, 0.09$ ($\sim 3\sigma$), $0.18, 0.36, 0.75, 1.5, 3.0, 7.5, 15.0$, and 30 mJy beam^{-1} . The convolved 18 arcsec beam is shown in the bottom left corner of each panel. The galaxy name and heliocentric velocity (all but one, ESO233-IG004, from HIPASS) are also displayed. The velocity of ESO233-IG004 is taken from Jones *et al.* (2009).

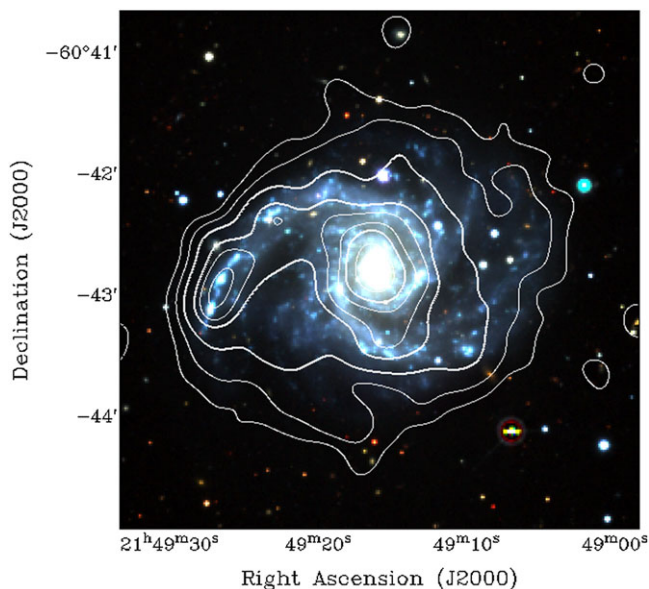


Figure 27. DES-DR1 optical composite image of the nearby face-on spiral galaxy NGC 7125 overlaid with contours from the EMU-PS. The contour levels are: 0.1, 0.25, 0.5, 1.0, 1.3, 1.6, 2.0, and 2.4 mJy beam⁻¹. NGC 7125 and its neighbour NGC 7216 form an interacting galaxy pair (HIPASS J2149-60) with a large pool of hydrogen gas for star formation.

our preliminary measurements allow us to quantify the fraction of 6dFGS galaxies that are radio sources and allows us to push fainter than blind radio source catalogues. Of the 2506 6dFGS galaxies in the EMU-PS region, 1887 (75%) have a flux density greater than 75 μ Jy beam⁻¹, corresponding to $\gtrsim 3\sigma$. As SFGs and passive galaxies have different distributions of radio continuum luminosities, we roughly split these two populations using the presence and absence of H α , measured from the 6dFGS spectra (Jones et al. 2004; 2009). To quantify noise and source confusion, we also measure flux density at positions offset by 100 pixels (200 arcsec, so well outside the relevant galaxy).

In Figure 29, we present the histogram of EMU-PS flux densities of 6dFGS galaxies with H α and with $K < 12.65$, along with the histogram of flux densities measured at offset positions. Roughly half of the SFGs are fainter than 1 mJy and would not have been detected by previous generations of wide-field radio continuum surveys. Almost all 6dFGS galaxies with detectable H α emission and $K < 12.65$ in the EMU-PS area are detected, with just 17 of the 623 galaxies having flux densities below 75 μ Jy. For comparison, at the 623 offset positions there are just 22 flux density measurements brighter than 75 μ Jy beam⁻¹ (corresponding to $\gtrsim 3\sigma$) and only 8 flux density measurements brighter than 125 μ Jy beam⁻¹ (corresponding to $\gtrsim 5\sigma$).

The radio continuum flux densities of $K < 12$ galaxies with and without H α emission is presented in Figure 30. Most $K < 12$ SFGs are detected by EMU-PS, and a significant fraction of passive galaxies are also detected. While the lowest mass passive galaxies are often undetected by EMU-PS, all but one of the $M_K < -26$ passive galaxies has a positive radio continuum flux density, presumably resulting from AGNs. This is consistent with Brown et al. (2011) and Sabater et al. (2019), who have concluded that all massive elliptical galaxies are radio continuum sources, using NVSS and LOFAR, respectively. When complete, EMU will detect thousands of nearby $M_K < -26$ elliptical galaxies, enabling

characterisation of the radio luminosities of these objects and the AGNs they host.

6.6. Comparison with Gaia

The Gaia project (Gaia Collaboration et al. 2016) has measured the parallax and proper motion of over a billion stars, and as a byproduct has also identified a number of quasars and compact galaxies (Bailer-Jones et al. 2019). To produce a catalogue of candidate radio-loud quasars, we therefore cross-match the DES counterparts to EMU radio sources against the Gaia EDR3 catalogue (Gaia Collaboration et al. 2021). We use the same technique as in earlier cross-matches in this paper, resulting in a plot of cross-matches as a function of search radius for shifted and unshifted data, shown in Figure 31. As a result of this test, we choose a cross-match radius of 0.2 arcsec, resulting in 14 174 cross-matches in the unshifted data, and 14 cross-matches in the shifted data, indicating a false-ID rate of 0.1%.

To explore the infrared properties of this sample of Gaia-selected sources, we need to use the WISE W3 band, which is absent from the CWISE catalogue, and so we must match our sources against the AllWISE catalogue (Cutri et al. 2021). We therefore cross-match the list of 14 174 sources, using a search radius of 1 arcsec, against the AllWISE catalogue, resulting in a catalogue of 11 142 sources with WISE W1, W2, and W3 flux densities. These sources are shown in Figure 32, colour-coded by their proper motion.

The sources with the lowest proper motions lie in the region identified by Jarrett et al. (2017) as being dominated by quasars, while a higher level of proper motion is seen in the region dominated by galaxies. This effect was also noted by Bailer-Jones et al. (2019) who explained it as extended galaxies not having well-defined centroids, causing the measured Gaia position to vary, resulting in an apparent proper motion. The group with the highest proper motion (coded as yellow) lie in the region designated as stars, confirming that these DES sources are indeed stars. However, most, if not all, of these ‘stars’ are probably false IDs and do not correspond to radio sources.

Of the 11 142 galaxies with W1, W2, and W3 flux densities, 2604 have W1-W2 > 0.8 , and we refer to these as quasar candidates. To estimate the false-ID rate, we repeated the above selection process after shifting the declination by 1 arcmin, and this resulted in 2312 sources with W1, W2, and W3 flux densities, of which 503 have W1-W2 > 0.8 . We therefore expect that 81% of our quasar candidates are radio-loud quasars, assuming that no other types of source fall in that part of the WISE colour diagram.

The combination of the Gaia selection and the WISE colour selection has, therefore, yielded a catalogue of 2312 radio-loud quasar candidates, of which about 81% are true radio-loud quasars. Using the same technique on the entire EMU survey will yield a catalogue of about 230 000 radio-loud quasar candidates, representing a significant increase in the number of known radio-loud quasars.

6.7. Clusters of galaxies

Galaxy clusters represent some of the largest gravitationally bound structures in the universe, and radio emission provides an insight into their formation and evolution. They evolve and grow through a variety of processes including passive accretion of gas,

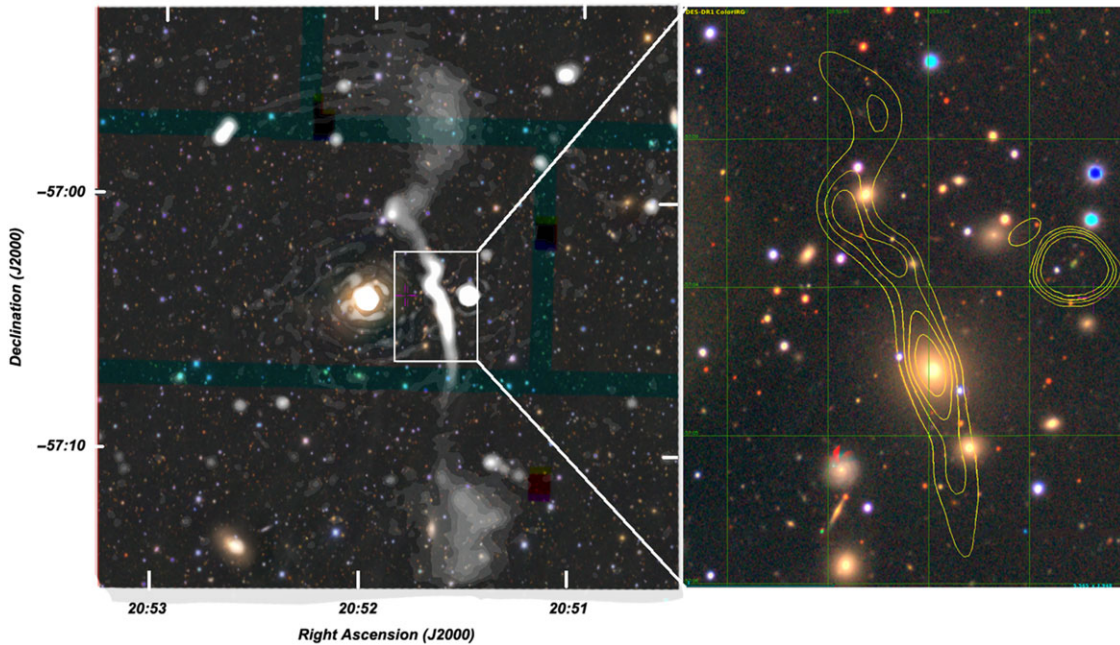


Figure 28. (Left) The Giant Radio Galaxy (GRG) EMU PS J205139.8–570434, with radio (at native resolution) shown in greyscale, overlaid on the DES DR1 colour image. The GRG consists of the roughly north-south jet and the two diffuse plumes above and below it. The strong source to the east, surrounded by diffraction rings, is the well-studied galaxy IC 5063. (Right) A contour diagram of the central part of the GRG at 18 arcsec resolution, overlaid on the DES DR1 colour image. Contour levels are 3, 7, 12, and 18 mJy beam⁻¹.

consumption of small galaxy groups, and violent merger events which can deposit vast amounts of energy ($\sim 10^{64}$ erg, e.g. Ferrari *et al.* 2008) into the ICM.

Many merging galaxy clusters host vast and enigmatic radio continuum sources. These diffuse radio sources are broadly classified into two categories: radio relics (or cluster radio shocks) and radio halos (see van Weeren *et al.* 2019, for a recent review). To date, some ~ 70 clusters are known to host radio relics, and some ~ 65 clusters are known to host radio halos^j.

Radio relics are highly extended (typically ~ 1 Mpc), highly polarised, diffuse synchrotron sources that lie towards the periphery of galaxy clusters. They often exhibit curved morphologies and filamentary sub-structures and are thought to be powered by shocks which generate relativistic electrons through a form of diffusive shock acceleration.

Radio halos, on the other hand, are largely amorphous, unpolarised diffuse synchrotron sources that are centrally located in merging galaxy clusters, and roughly follow the distribution of the thermal plasma in the ICM (as traced by X-ray emission). The most commonly accepted scenario is that radio halos are powered by turbulence injected in the ICM during cluster merger events, although there are alternatives based on collisions between cosmic ray protons (CRp) and thermal protons from the ICM (for a review, see Brunetti & Jones 2014). On smaller scales ($\lesssim 0.5$ Mpc), ‘mini-halos’ are relatively small diffuse radio sources that are generally co-located with powerful, radio-loud, brightest cluster galaxies (BCGs) in relaxed clusters. One theoretical explanation for mini-halos is that ‘core-sloshing’ in the ICM from minor or off-axis mergers produces small-scale turbulence which can then provide sufficient energy for re-acceleration of the relativistic electrons.

For relics, halos, and mini-halos, the shape of the synchrotron emitting spectrum provides a diagnostic for these relativistic particle (re-)acceleration processes. Historically, our understanding of the relevant physics has been limited by (i) the generally relatively poor quality of low-frequency radio data, (ii) missing short spacings, leading to loss of highly-extended radio emission, and (iii) narrow bandwidths, limiting the spectral shape measurements. By circumventing these limitations with the EMU survey, the sample of clusters suitable for study can be increased by at least two orders of magnitude.

There are already ~ 20 known X-ray detected galaxy clusters in the EMU-PS area. All show compact or moderately extended radio sources that are likely associated with AGN. The eROSITA survey (Predehl *et al.* 2021) will provide many more X-ray clusters for radio investigation. The first eROSITA all-sky survey (eRASS1) will find as many as 1.5 clusters/deg²; more than 3 clusters/deg² are expected after all eight all-sky surveys are completed (e.g., Pillepich *et al.* 2018). Hence, we expect as many as 400 X-ray-detected clusters will soon be available in the EMU-PS area alone, and more than 10 000 AGN.

Early EMU/eROSITA results on the Abell 3391/95 galaxy cluster system (Reiprich *et al.* 2021; Brügggen *et al.* 2021) have already helped constrain physical processes in the merger. We show two additional examples of diffuse radio sources detected in the EMU-PS area in Figures 33 and 34.

Other cluster catalogues will similarly provide important targets for EMU-PS and the full EMU Survey. For example, Aguena *et al.* (2021) provide the WazP catalogue of 60542 clusters from the DES^k. About 30 of their BCGs are coincident with extended RGs in the EMU-PS and will be discussed by Andernach *et al.* (in preparation).

^jAn up-to-date database of these sources is maintained at [GalaxyClusters.com](https://galaxyclusters.com).

^k<https://www.linea.gov.br/catalogs/wazp/>

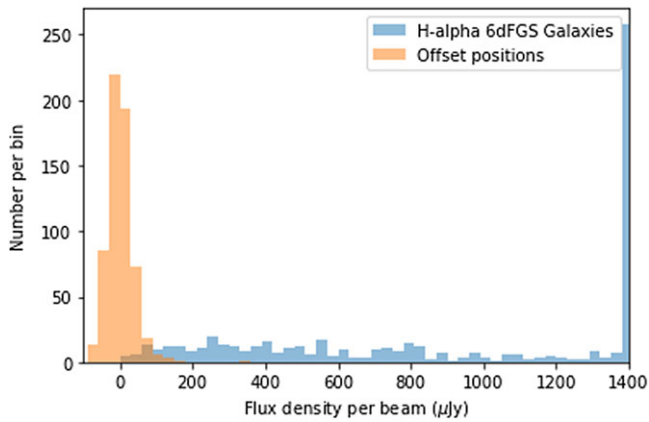


Figure 29. The histogram of EMU-PS flux densities for 6dFGS galaxies with H α emission and $K < 12.65$, along with the corresponding histogram of flux densities measured at offset positions. Just 17 of the 623 6dFGS galaxies with detectable H α emission have radio flux densities below $75 \mu\text{Jy beam}^{-1}$.

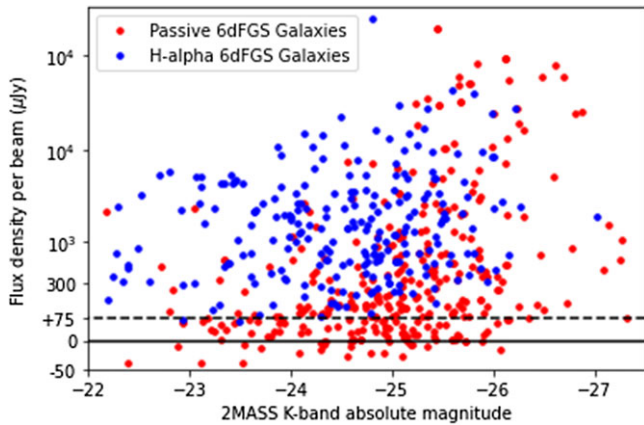


Figure 30. The EMU-PS flux densities of $K < 12$ galaxies with and without H α emission as a function of absolute magnitude. The dashed line shows $75 \mu\text{Jy}$, roughly corresponding to 3σ . Almost all star-forming galaxies are detected by the EMU-PS. While low mass passive galaxies can have no detectable radio continuum emission, all but one $M_K < -26$ passive galaxy has a positive radio continuum flux density.

6.7.1. SPT-CL J2023-5535

Figure 33 presents the radio halo and relic in the massive merging galaxy cluster, SPT-CL J2023–5535 ($z = 0.23$), reported by HyeongHan et al. (2020). Their weak-lensing analysis has revealed significant substructure in this massive ($M_{200} = 1.04 \pm 0.36 \times 10^{15} M_{\odot}$) cluster, which comprises three subclusters.

The merger event between the eastern and central subclusters appears to have generated a ~ 0.5 Mpc radio relic on the western edge of the central subcluster. The results presented by HyeongHan et al. (2020) show an unusually flat spectral index $\alpha_{\text{int}} = -0.76 \pm 0.06$, which may indicate that this relic is powered by the re-acceleration of fossil electrons, perhaps originally seeded by a nearby (photometric) cluster member AGN. Follow-up observations at other radio frequencies will be required to confirm this flat spectrum.

6.7.2. SPT-CL J2032-5627

Figure 34 shows a rare class of a possible double-radio relic with an elongation of X-ray emission in the massive ($M_{500} = 4.77^{+0.71}_{-0.63} \times 10^{14} M_{\odot}$; Bulbul et al. 2019) cluster SPT-CL J2032–5627

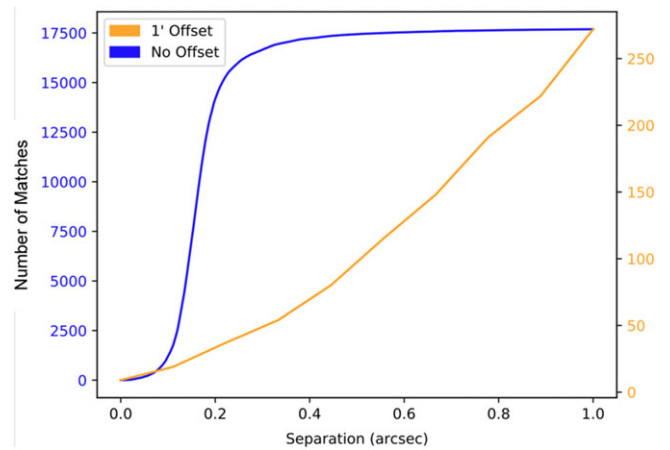


Figure 31. The number of cross-matches between DES counterparts to EMU-PS sources, and Gaia sources, for unshifted data (blue), and data shifted by one arcmin (orange).

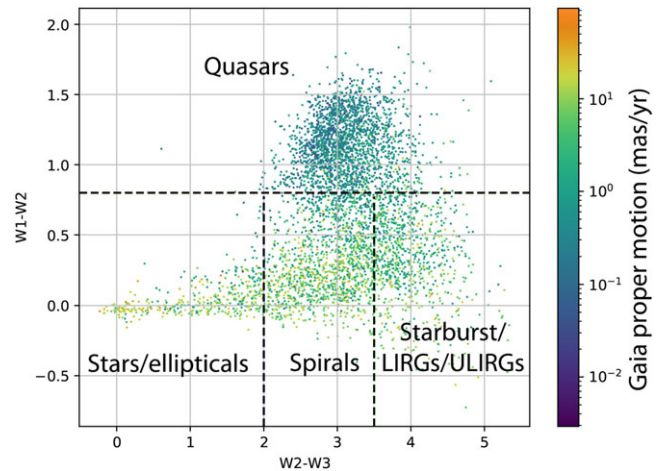


Figure 32. The AllWISE colour-colour plot for EMU-PS sources cross-matched with Gaia, colour-coded according to their measured proper motion. The dashed lines divide the graph into the regions identified by Jarrett et al. (2017).

($z = 0.28$). The north-western (sources A & B) and south-eastern (source C) all exhibit steep radio spectra ($\alpha_{\text{int}} = -1.75$, $\alpha_{\text{int}} = -1.69$, and $\alpha_{\text{int}} = -1.46$, respectively).

The highly asymmetric X-ray surface brightness profile and large projected separation between the radio relics in this cluster suggest that the merger event is occurring close to the plane of the sky. Curiously, no evidence of a shock has been found in the X-ray surface brightness. However, the presence of a cold front towards the leading edge to the south-east of the cluster may suggest that the lack of a shock detection is due to the relatively shallow depth (25 ks) of the existing XMM-Newton observations. See also Duchesne et al. (2021) for further discussion of SPT-CL J2032–5627.

6.7.3. A Mini-Halo in a poor cluster

Figure 35 shows a very low surface brightness structure, much fainter ($50 \mu\text{Jy beam}^{-1}$) than the embedded compact 14.8 ± 0.07 mJy source associated with 6dFGS g2212485-614658 at a redshift of $z=0.054$. The low surface brightness emission was found using the multi-resolution filtering technique of Rudnick

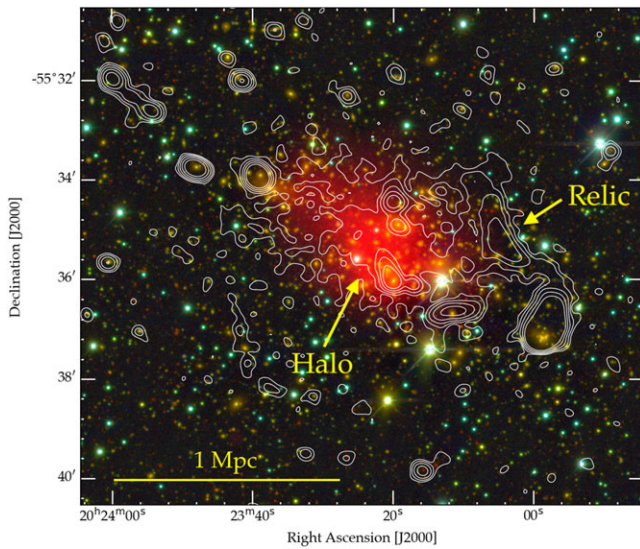


Figure 33. Multi-wavelength composite image of SPT-CL J2023–5535. Contours denote the EMU-PS surface brightness at 944 MHz at 18 arcsec resolution, at $3\sigma_{rms} \times 2^n$ where $n = 0, 1, 2, 3, 4$ and $\sigma_{rms} \approx 25 \mu\text{Jy beam}^{-1}$. Background colourmap shows a composite g , r , and i image from DECam. X-ray emission from *Chandra* is also overlaid in red. New diffuse radio sources identified by HyeonHan et al. (2020) are also indicated.

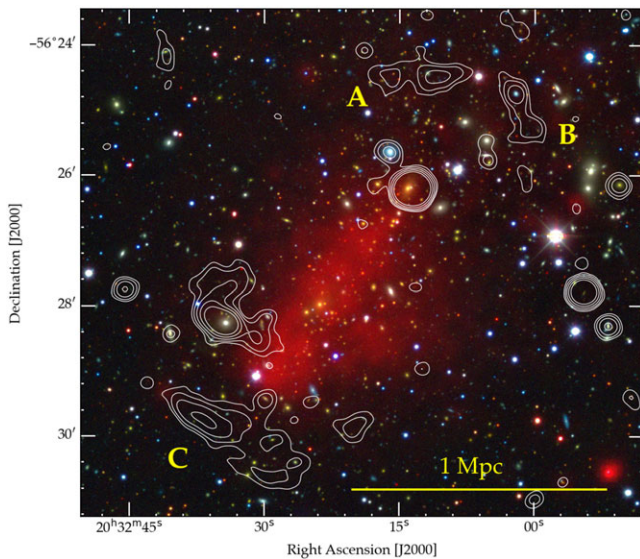


Figure 34. Multi-wavelength composite image of the cluster SPT-CL J2032–5627. Colour map and contours are the same as Figure 33, but with 25 ks XMM-*Newton* surface brightness shown in red. It appears that the cluster hosts one of the rare class of double-radio relics with the northern (A and B) and southern (C) relics as indicated.

(2002), using a filter box size of 34 arcsec which removes the emission from compact components. It has a total extent of 150 arcsec (160 kpc) and a total flux density of 5 ± 0.5 mJy, corresponding to a luminosity of $\approx 3 \times 10^{22}$ W/Hz. No substructure is apparent.

The diffuse structure could be the dying remains of a radio galaxy, faded to a luminosity comparable to the faintest AGN or to typical SFGs (Mauch & Sadler 2007). The lack of radio structure, however, suggests that it could also be an underluminous mini-halo, an option we briefly explore here.

There is no catalogued cluster associated with 6dFGS g2212485-614658, although there are five galaxies with a similar

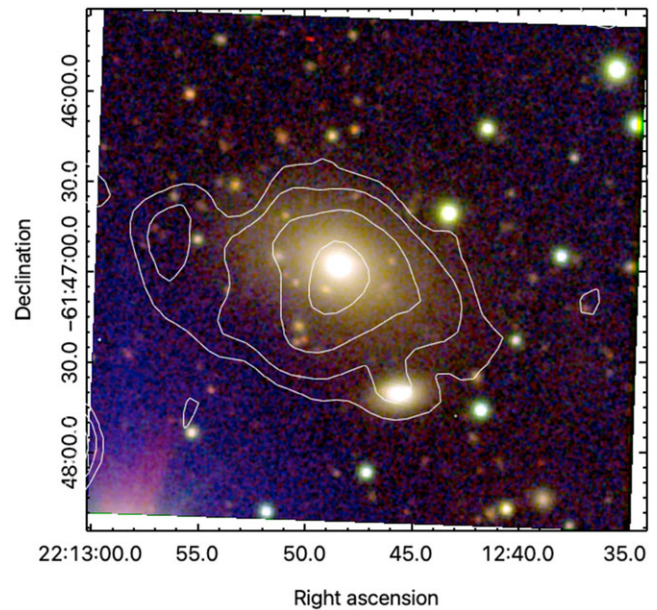


Figure 35. Radio contours overlaid on a multi-wavelength (irg) composite image of 6dFGS g2212485-614658 from DES. The radio image was made from the EMU-PS native resolution data by subtracting four unresolved sources and then convolving to a resolution of 18 arcsec. Contours are at 75, 150, 300, and 600 $\mu\text{Jy beam}^{-1}$. The subtracted sources were at 22:12:48.64 – 61:46:58.5 (14.9 mJy), 22:12:43.04 – 61:46:50.1 (0.3 mJy), 22:12:51.19 – 61:46:15.5 (0.2 mJy), 22:12:37.17 – 61:47:24.5 (0.1 mJy)

redshift listed in Vizier, out to a separation of 17 arcmin (1 Mpc). This, and the presence of many smaller galaxies embedded in the 6dFGS g2212485-614658 envelope (Figure 35) suggest that this could be a poor cluster or group.

The radio and extended (as opposed to AGN) X-ray luminosities of mini-halo systems are well correlated (Giacintucci et al. 2019). For this system, we determined upper limits to the bolometric (0.2–2 keV) X-ray emission using both RASS and XMM Slew archives, yielding limits in the range $1.4\text{--}2.4 \times 10^{-13}$ erg/s/cm². At mid-range, the inferred luminosity upper limit of 10^{42} erg/s is two orders of magnitude lower than that of the mini-halo clusters summarised in Giacintucci et al. (2019) and than the value expected from the radio-X-ray correlation.

Probing mini-halo-like structures in these poor-cluster, low X-ray luminosity type systems is important for understanding the physical mechanisms which form and continue to power the radio emission. We do not know whether the current observed radio-X-ray correlation is influenced by X-ray selection effects, or whether the correlation breaks down at very low cluster masses.

The sensitivity of EMU to very low surface brightness emission such as presented here will provide a powerful tool for exploring the connection between compact and extended AGN emissions and pure cluster/group particle acceleration processes in mini-halos.

6.8. Cosmology

The spatial distribution of radio sources is a tracer of the underlying matter distribution and can be used to probe the formation conditions of radio galaxies, as well as the underlying fundamental ingredients and physics of the universe. As these continuum sources are not easy to localise in redshift, we use measurements of angular clustering for the EMU-PS.

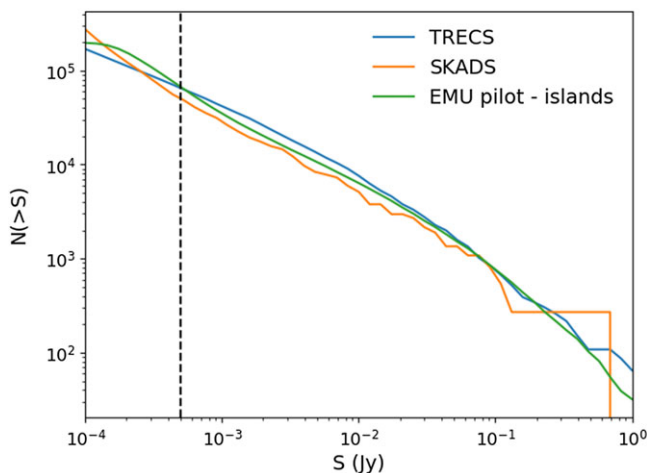


Figure 36. The number of sources in the EMU-PS with a flux density greater than some limit (S), as a function of that limit, compared to scaled predictions from the SKADS and T-RECS simulated catalogues. The dashed black vertical line gives the $500\mu\text{Jy}$ limit we assume for the clustering analysis presented in this paper. There is some discretisation of the prediction for the larger flux density limits, due to a scaling of some small integer value for the original prediction that was made for a much smaller value.

Here, we use the Landy & Szalay (1993) estimator, which is defined as:

$$w_{\text{LS}}(\theta) = \frac{DD(\theta) + RR(\theta) - 2DR(\theta)}{RR(\theta)}, \quad (1)$$

where $DD(\theta)$ is the number of observed galaxy pairs at distance between θ and $\theta + d\theta$, $RR(\theta)$ is the number of random galaxy pairs at this separation, and $DR(\theta)$ is the number of observed random pairs. We apply this statistic to the pilot survey catalogue, using the island data catalogue as the data vector (D), and generated random catalogues (R), normalising the number over all angles such the angular correlation function $w(\theta)$ functions as a probability excess or decrement relative to an entirely random distribution of galaxies on the sky.

The random catalogue (R) is generated using the method used in Hale et al. (2018) and Siewert et al. (2020) where random positions for simulated sources are generated across the EMU-PS field of view and for each simulated source a flux density is randomly assigned to the source using flux densities from the SKADS simulation (Wilman et al. 2008)¹. We assign noise to the flux density of the simulated source by sampling from a Gaussian distribution with spread given by the RMS at the random source location. A source remains within the random catalogue provided the simulated source peak flux density (where we assume the random sources are unresolved) added to the noise would be detectable at $\geq 5 \times$ the RMS at the simulated source position.

The robustness of this approach to generate the randoms is checked by comparing the fluxes of the simulated catalogues to the island catalogue of the EMU-PS. We selected both AGN and SFG galaxies from SKADS and T-RECS (Bonaldi et al. 2019) simulations. In Figure 36, we compare the number counts for different flux density cuts $N(>S)$ between the EMU-PS island catalogue

¹We use the SKADS 1.4 GHz flux scaled to 944 MHz assuming a spectral index of -0.8. We also apply a minimum flux density cut on the 944 MHz converted SKADS flux of $\sim 30\mu\text{Jy beam}^{-1}$

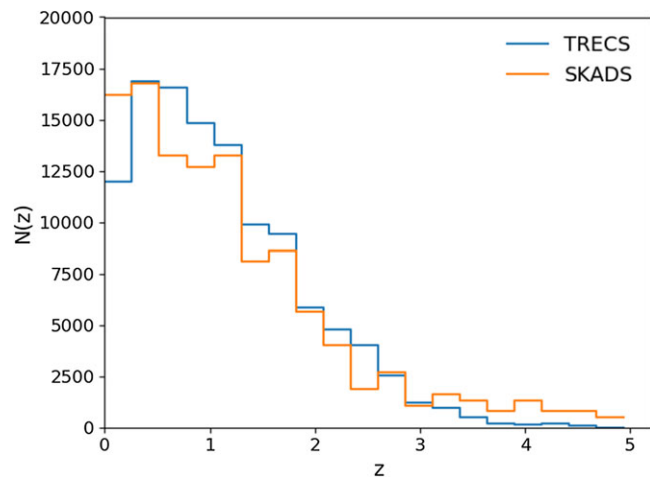


Figure 37. The predicted number of sources in the EMU Pilot Survey as a function of redshift, generated by scaling the predictions from the SKADS and T-RECS simulated catalogues. This assumes a flux density limit of $500\mu\text{Jy}$

and the number counts from both simulated radio catalogues at 1 GHz.

In order to calculate the expected $w_{\text{LS}}(\theta)$ distribution, we must know the redshift distribution $N(z)$ of the sources. For the analysis here, the SKADS and T-RECS simulations are used for $N(z)$ and are shown in Figure 37. There is good agreement in the redshift distribution between these two catalogues, and this consistency indicates that we are accurately modelling $N(z)$ and choosing the SKADS catalogue should not introduce a significant error. Using the $N(z)$ distribution estimated from SKADS, we compute the theoretical expectation for the clustering statistics at the flux density cut of $500\mu\text{Jy}$.

The measured angular correlation function $w(\theta)$ is shown in Figure 38, estimating the errors from bootstrap resampling the data and random simulated data 100 times. We also show the predicted angular correlation function, assuming a cosmological model with values fixed at the values listed in Table 2, with a number distribution and bias model from SKADS. We show that the theoretical prediction, with no tuning of free parameters, is a reasonable fit to the data in the angular range $0.1^\circ < \theta < 10^\circ$. There is somewhat of a discrepancy at small scales ($\theta < 0.1^\circ$), which is probably generated by the multiple components that can be generated by the same radio galaxy, but which here are being treated as independent tracers of the cosmological density field. A more complete analysis, including calibration of the effect of multi-component sources on the angular correlation function on small scales, is planned for future work.

6.9. The excess of flat spectral index sources

To investigate the skew towards flatter and inverted spectral indices shown in Figures 10 and 11, we compare the spectral index distributions for a sample of clearly resolved and unresolved components from the EMU-PS. The unresolved population contains radio cores and therefore includes flat-spectrum radio quasars (Urry & Padovani 1995) and peaked-spectrum sources (O’Dea & Saikia 2021). At the observing frequency of EMU-PS ($\nu \sim 900$ MHz), the radio spectra of Gigahertz Peaked-Spectrum sources tend to have shallow spectral index values as EMU-PS is observing close to their turnover frequency (O’Dea 1998). For this

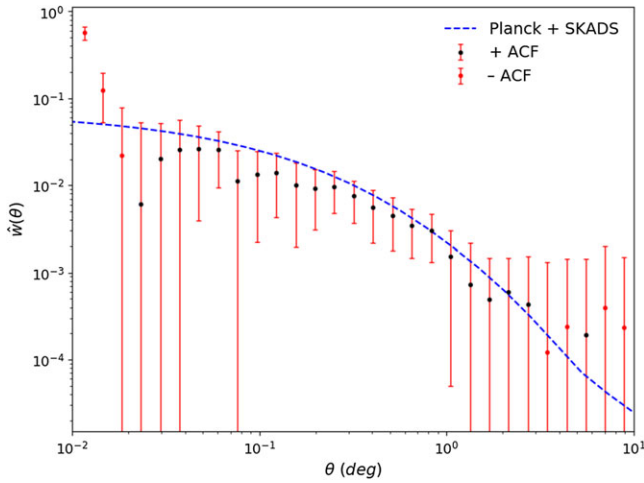


Figure 38. The measured angular correlation function (ACF) $w(\theta)$ as a function of angular separation with one-sigma error bar computed from bootstrap re-sampling from 100 bootstraps. The correlation function is measured from the integrated flux-corrected EMU-PS island catalogue, using all sources above a flux density limit of $500\mu\text{Jy}$. The blue curve is the theoretical prediction for the correlation function, assuming the Planck 2018 best fit cosmology and a SKADS model for the number distribution with redshift and the bias. No fitting of the cosmological or bias parameters was performed to change the prediction curve. As negative values cannot be shown on a log scale, in bins where the ACF becomes negative, we show (in red) the value of (-ACF) instead.

comparison, we define each source to be resolved or unresolved using the component size after deconvolution from the beam, Ψ , considering components with $\Psi < 2$ arcsec to be unresolved and components with $\Psi > 20$ arcsec to be resolved.

In Figure 39, we show the spectral index distributions for the resolved and unresolved EMU components at three levels of minimum peak brightness: $S_{\text{peak}} > 1 \text{ mJy beam}^{-1}$, $S_{\text{peak}} > 3 \text{ mJy beam}^{-1}$, and $S_{\text{peak}} > 10 \text{ mJy beam}^{-1}$. Resolved components have symmetric distributions around a peak of $\alpha \sim -0.7$. However, while the spectral index distribution for the unresolved population is comparable to the resolved population at steep negative spectral indices ($\alpha < -0.7$), the distributions differ at flatter spectral indices. At $\alpha > -0.7$, the unresolved population dominates over the resolved population at all three brightness levels. Due to the large scatter in the spectral index distribution at sub-mJy levels (Figure 10), we have only performed this analysis on EMU components with $S_{\text{peak}} > 1 \text{ mJy beam}^{-1}$. Future EMU data, where potential issues in the spectral index calibration at lower signal to noise are better understood, will present the opportunity to study the spectral index distributions of fainter resolved and unresolved components. Such an analysis, particularly for the full EMU survey, will enable tests of the potential flattening of the spectral index distribution for radio sources with $S \lesssim 0.5 \text{ mJy}$ (Prandoni et al. 2006; Whittam et al. 2013).

The different spectral index distributions of resolved and unresolved components we observe with the EMU-PS are consistent with what is seen with higher angular resolution and higher frequency observations. Recently, Gordon et al. (2021) demonstrated the 1.4 – 3 GHz spectral index distributions for point-like radio components are skewed to flatter values than well-resolved components using observations from the Faint Images of the Radio Sky at Twenty cm survey (FIRST; $\nu \sim 1.4 \text{ GHz}$, Becker et al. 1995) and the Very Large Array Sky Survey (VLASS, $\nu \sim 3 \text{ GHz}$, Lacy et al. 2020). Further comparisons between EMU and radio

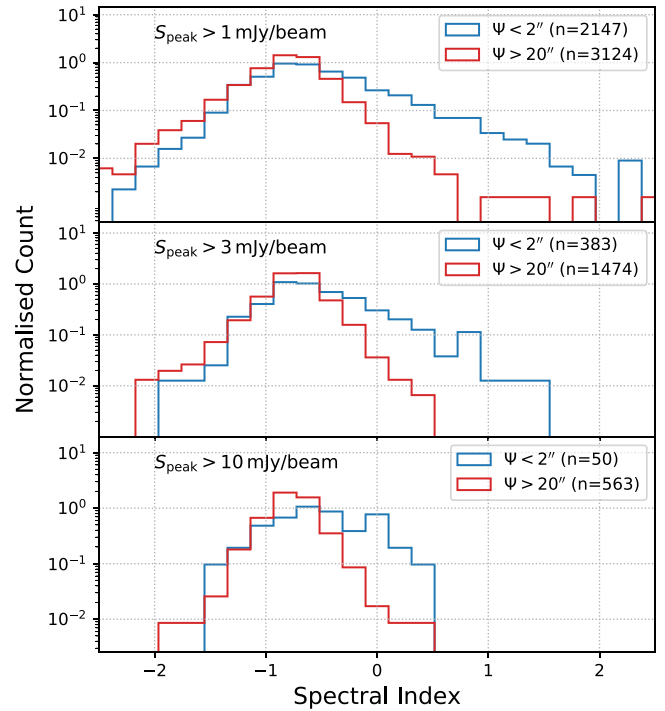


Figure 39. The spectral index distributions for unresolved ($\Psi < 2''$, blue) and resolved ($\Psi > 20''$, red) EMU components. The three panels show different minimum brightness levels, corresponding to $S_{\text{peak}} > 1 \text{ mJy beam}^{-1}$, $S_{\text{peak}} > 3 \text{ mJy beam}^{-1}$, and $S_{\text{peak}} > 10 \text{ mJy beam}^{-1}$ from top to bottom. The legend in each panel denotes the number of components contributing to each distribution shown. Each plot is normalised to the area under the curve.

observations in other bands, such as those from VLASS and the Australia Telescope Large Area Survey (ATLAS, 1.4 – 2.3 GHz, Zinn et al. 2012), may help quantify the fractions of peaked-spectrum sources with different turnover frequencies, and this will be the focus of a follow-up work.

7. Conclusion

We have presented the first pilot survey of EMU, using the ASKAP telescope.

The resulting images reach an rms sensitivity of about $25\text{--}30 \mu\text{Jy beam}^{-1}$ rms at a spatial resolution of $\sim 11\text{--}18$ arcsec and result in a catalogue of $\sim 220\,000$ sources, of which $\sim 180\,000$ are compact. We have presented the catalogue of compact sources, together with optical and infrared cross-identifications and redshifts. We have also shown some preliminary science results, on both these compact sources and on diffuse sources, which will be discussed in more detail in subsequent papers.

The results presented here testify to the outstanding observational characteristics of ASKAP, including its high survey speed and unprecedented sensitivity to low surface brightness emission. Nevertheless, at the time of the pilot survey, several aspects of ASKAP correlator operation, calibration, and data processing were incomplete. We therefore expect future results from ASKAP, including the main EMU survey, to have even better sensitivity and dynamic range than the results presented in this paper.

Acknowledgements. We thank an anonymous referee for valuable feedback on an earlier iteration of this paper. The Australian SKA Pathfinder

is part of the Australia Telescope National Facility which is managed by CSIRO. Operation of ASKAP is funded by the Australian Government with support from the National Collaborative Research Infrastructure Strategy. Establishment of the Murchison Radio-astronomy Observatory was funded by the Australian Government and the Government of Western Australia. ASKAP uses advanced supercomputing resources at the Pawsey Supercomputing Centre. We acknowledge the Wajarri Yamatji people as the traditional owners of the Observatory site. This work makes use of data products from the Wide-field Infrared Survey Explorer, which is a joint project of the University of California, Los Angeles, and the Jet Propulsion Laboratory/California Institute of Technology, funded by the National Aeronautics and Space Administration. It also makes use of data from the European Space Agency (ESA) mission Gaia, and we acknowledge the institutions listed on https://gea.esac.esa.int/archive/documentation/GEDR3/Miscellaneous/sec/_acknow/. It also uses public archival data from the DES and we acknowledge the institutions listed on <https://www.darkenergysurvey.org/the-des-project/data-access/>. This research has made use of the ‘Aladin sky atlas’ developed at CDS, Strasbourg Observatory, France (Boch & Fernique 2014). This research uses services or data provided by the Astro Data Lab at NSF’s National Optical-Infrared Astronomy Research Laboratory. NOIRLab is operated by the Association of Universities for Research in Astronomy (AURA), Inc. under a cooperative agreement with the National Science Foundation. Partial support for LR comes from US National Science Foundation Grant AST 17-14205 to the University of Minnesota. The National Radio Astronomy Observatory is a facility of the National Science Foundation operated under cooperative agreement by Associated Universities, Inc. CLH acknowledges support from the Leverhulme Trust through an Early Career Research Fellowship. IP acknowledges support from CSIRO under its Distinguished Research Visitor Programme, and from INAF through the SKA/CTA PRIN “FORECaST” and the PRIN MAIN STREAM “SAuROS” projects. MJJ acknowledges support from the National Research Foundation of Korea under the program nos. 2017R1A2B2004644 and 2017R1A4A1015178. CJR acknowledges financial support from the ERC Starting Grant ‘DRANOEL’, number 714245. HA benefited from grant CIIC 174/2021 of Universidad de Guanajuato.

References

- Abbott, T. M. C., et al. 2018, *ApJS*, **239**, 18
- Afonso, J., et al. 2011, *ApJ*, **743**, 122
- Agüena, M., et al. 2021, *MNRAS*, **502**, 4435
- Bailer-Jones, C. A. L., Fouesneau, M., & Andrae, R. 2019, *MNRAS*, **490**, 5615
- Barnes, D. G., et al. 2001, *MNRAS*, **322**, 486
- Becker, R. H., White, R. L., & Helfand, D. J. 1995, *ApJ*, **450**, 559
- Bera, A., Kanekar, N., Chengalur, J. N., & Bagla, J. S. 2019, *ApJ*, **882**, L7
- Bilicki, M., et al. 2016, *ApJS*, **225**, 5
- Boch, T., & Fernique, P. 2014, in *Astronomical Data Analysis Software and Systems XXIII*, ed. N. Manset, & P. Forshay, Astronomical Society of the Pacific Conference Series, vol. 485, 277
- Bock, D. C. J., Large, M. I., & Sadler, E. M. 1999, *AJ*, **117**, 1578
- Boller, T., Freyberg, M. J., Trümper, J., Haberl, F., Voges, W., & Nandra, K. 2016, *A&A*, **588**, A103
- Bonaldi, A., Bonato, M., Galluzzi, V., Harrison, I., Massardi, M., Kay, S., De Zotti, G., & Brown, M. L. 2019, *MNRAS*, **482**, 2
- Bondi, M., Ciliegi, P., Schinnerer, E., Smolčić, V., Jahnke, K., Carilli, C., & Zamorani, G. 2008, *ApJ*, **681**, 1129
- Bonnarel, F., et al. 2000, *A&AS*, **143**, 33
- Brienza, M., et al. 2017, *A&A*, **606**, A98
- Briggs, D. S. 1995, PhD thesis, New Mexico Institute of Mining and Technology Socorro, New Mexico
- Brown, M. J. I., Jannuzi, B. T., Floyd, D. J. E., & Mould, J. R. 2011, *ApJ*, **731**, L41
- Brüggen, M., et al. 2021, *A&A*, **647**, A3
- Brunetti, G., & Jones, T. W. 2014, *Int. J. Mod. Phys. D*, **23**, 1430007
- Bulbul, E., et al. 2019, *ApJ*, **871**, 50
- Burenin, R. A., Vikhlinin, A., Hornstrup, A., Ebeling, H., Quintana, H., & Mescheryakov, A. 2007, *ApJS*, **172**, 561
- Calabretta M. R., Staveley-Smith L., Barnes D. G., 2014, *PASA*, **31**, e007
- Chapman, J. M., Dempsey, J., Miller, D., Heywood, I., Pritchard, J., Sangster, E., Whiting, M., & Dart, M. 2017, in *Astronomical Data Analysis Software and Systems XXV*, ed. N. P. F. Lorente, K. Shorridge, & R. Wayth, Astronomical Society of the Pacific Conference Series, vol. 512, 73
- Condon, J. J. 1992, *ARA&A*, **30**, 575
- Condon, J. J., Cotton, W. D., Greisen, E. W., Yin, Q. F., Perley, R. A., Taylor, G. B., & Broderick, J. J. 1998, *AJ*, **115**, 1693
- Condon, J. J., Cotton, W. D., & Broderick, J. J. 2002, *AJ*, **124**, 675
- Cornwell, T. J., Golap, K., & Bhatnagar, S. 2008, *IEEE J. Selected Top. Sig. Process.*, **2**, 647
- Cotton, W. D., et al. 2020, *MNRAS*, **495**, 1271
- Cutri, R. M., et al. 2021, *VizieR Online Data Catalog*, p. II/328
- Dahlem, M., Ehle, M., Ryder, S. D., Vlajić, M., & Haynes, R. F. 2005, *A&A*, **432**, 475
- Davies, L. J. M., et al. 2017, *MNRAS*, **466**, 2312
- Drlica-Wagner, A., et al. 2018, *ApJS*, **235**, 33
- Duchesne, S. W., Johnston-Hollitt, M., Bartalucci, I., Hodgson, T., & Pratt, G. W. 2021, *PASA*, **38**, e005
- Eddington, A. S. 1913, *MNRAS*, **73**, 359
- Eddington, A. S. 1940, *MNRAS*, **100**, 354
- Ekers, R. D. 1970, *AuJPh*, **23**, 217
- Fanaroff, B. L., & Riley, J. M. 1974, *MNRAS*, **167**, 31P
- Ferrand, G. 2019, Slicing the LCH space, Available at <https://nbviewer.jupyter.org/github/gillesferrand/colourspace/blob/master/4.slices.ipynb> (accessed 10 May 2021)
- Ferrari, C., Govoni, F., Schindler, S., Bykov, A. M., & Rephaeli, Y. 2008, *SSRv*, **134**, 93
- Gaia Collaboration et al. 2016, *A&A*, **595**, A2
- Gaia Collaboration et al. 2021, *A&A*, **649**, A1
- Giacintucci, S., Markevitch, M., Cassano, R., Venturi, T., Clarke, T. E., Kale, R., & Cuciti, V. 2019, *ApJ*, **880**, 70
- Gordon, Y. A., et al. 2021, arXiv e-prints, p. arXiv:2102.11753
- Gregory, P. C., Vavasour, J. D., Scott, W. K., & Condon, J. J. 1994, *ApJS*, **90**, 173
- Guzman, J., et al. 2019, ASKAPsoft: ASKAP science data processor software (ascl:1912.003)
- Hale, C. L., Jarvis, M. J., Delvecchio, I., Hatfield, P. W., Novak, M., Smolčić, V., & Zamorani, G. 2018, *MNRAS*, **474**, 4133
- Hay, S., O’Sullivan, J., Kot, J., & Granet, C. 2006, in *The European Conference on Antennas and Propagation: EuCAP 2006*, ed. H. Lacoste, & L. Ouweland, ESA Special Publication, vol. 626, 663
- Healey, S. E., Romani, R. W., Taylor, G. B., Sadler, E. M., Ricci, R., Murphy, T., Ulvestad, J. S., & Winn, J. N. 2007, *ApJS*, **171**, 61
- Heesen, V., Brinks, E., Leroy, A. K., Heald, G., Braun, R., Bigiel, F., & Beck, R. 2014, *AJ*, **147**, 103
- Heesen, V., Dettmar, R.-J., Krause, M., Beck, R., & Stein, Y. 2016, *MNRAS*, **458**, 332
- Heesen, V., et al. 2018, *MNRAS*, **474**, 5049
- Heywood, I., et al. 2016, *MNRAS*, **460**, 4433
- Hopkins, A. M., Afonso, J., Chan, B., Cram, L. E., Georgakakis, A., & Mobasher, B. 2003, *AJ*, **125**, 465
- Hotan, A. W., et al. 2021, *PASA*, **38**, e009
- Huynh, M., Dempsey, J., Whiting, M. T., & Ophel, M. 2020, in *Astronomical Data Analysis Software and Systems XXVII*, ed. Ballester P., Ibsen J., Solar M., Shorridge K., Astronomical Society of the Pacific Conference Series, vol. 522, 263
- HyeonHan, K., et al. 2020, *ApJ*, **900**, 127
- Ishwara-Chandra, C. H., & Saikia, D. J. 1999, *MNRAS*, **309**, 100
- Itten, J. 1970, *The Elements of Colour*. Van Nostrand Reinhold Company, Toronto
- Jarrett, T. H., et al. 2017, *ApJ*, **836**, 182
- Johnston, S., et al. 2007, *PASA*, **24**, 174
- Johnston, S., et al. 2008, *ExA*, **22**, 151
- Jones, P. A., & McAdam, W. B. 1992, *ApJS*, **80**, 137
- Jones, D. H., et al. 2004, *MNRAS*, **355**, 747
- Jones, D. H., et al. 2009, *MNRAS*, **399**, 683
- Koribalski, B. S., & López-Sánchez, A. R. 2009, *MNRAS*, **400**, 1749
- Koribalski, B. S., et al. 2004, *AJ*, **128**, 16

- Koribalski, B. S., et al. 2020, *Ap&SS*, **365**, 118
- Koribalski, B. S., Norris, R. P., Andernach, H., Rudnick, L., Shabala, S., Filipovic, M., & Lenc, E. 2021, *MNRAS*, **505**, L11
- Kuźmicz, A., Jamroz, M., Bronarska, K., Janda-Boczar, K., & Saikia, D. J. 2018, *ApJS*, **238**, 9
- Lacy, M., et al. 2020, *PASP*, **132**, 035001
- Landy, S. D., & Szalay A. S. 1993, *ApJ*, **412**, 64
- Leahy, D. A., et al. 2019, *PASA*, **36**, e024
- Mahatma, V. H., et al. 2018, *MNRAS*, **475**, 4557
- Mancuso, C., et al. 2017, *ApJ*, **842**, 95
- Mandal, S., et al. 2021, *A&A*, **648**, A5
- Marocco, F., et al. 2021, *ApJS*, **253**, 8
- Mauch, T., & Sadler, E. M. 2007, *MNRAS*, **375**, 931
- Mauch, T., Murphy, T., Buttery, H. J., Curran, J., Hunstead, R. W., Piestrzynski, B., Robertson, J. G., & Sadler, E. M. 2003, *MNRAS*, **342**, 1117
- McConnell, D., et al. 2016, *PASA*, **33**, e042
- McConnell, D., et al. 2019, *ASKAP Observation Guide*, Available at <https://confluence.csiro.au/display/askapsst/ASKAP+Observation+Guide> (accessed 10 May 2021)
- McConnell, D., et al. 2020, *PASA*, **37**, e048
- Meyer, M. J., et al. 2004, *MNRAS*, **350**, 1195
- Mocanu, L. M., et al. 2013, *ApJ*, **779**, 61
- Molnár, D. C., et al. 2021, *MNRAS*, **504**, 118
- Monroe, T. R., Prochaska, J. X., Tejos, N., Worseck, G., Hennawi, J. F., Schmidt, T., Tumlinson, J., & Shen, Y. 2016, *AJ*, **152**, 25
- Murphy, E. J. 2009, *ApJ*, **706**, 482
- Murphy, T., et al. 2010, *MNRAS*, **402**, 2403
- Murphy, E. J., et al. 2011, *ApJ*, **737**, 67
- Nawaz, M. A., Bicknell, G. V., Wagner, A. Y., Sutherland, R. S., & McNamara, B. R. 2016, *MNRAS*, **458**, 802
- Nordgren, T. E., Chengalur, J. N., Salpeter, E. E., & Terzian, Y. 1997, *AJ*, **114**, 913
- Norris, R. P. 2017a, *NatAs*, **1**, 671
- Norris, R. P. 2017b, *PASA*, **34**, e007
- Norris, R. P., et al. 2006, *AJ*, **132**, 2409
- Norris, R. P., et al. 2011, *PASA*, **28**, 215
- Norris, R. P., et al. 2021, *PASA*, **38**, e003
- O'Dea, C. P. 1998, *PASP*, **110**, 493
- O'Dea, C. P., & Saikia, D. J. 2021, *A&A Rev.*, **29**, 3
- Piffaretti, R., Arnaud, M., Pratt, G. W., Pointecouteau, E., & Melin, J. B. 2011, *A&A*, **534**, A109
- Pillepich, A., Reiprich, T. H., Porciani, C., Borm, K., & Merloni, A. 2018, *MNRAS*, **481**, 613
- Planck Collaboration et al. 2020, *A&A*, **641**, A6
- Prandoni, I., Gregorini, L., Parma, P., de Ruiter, H. R., Vettolani, G., Wieringa, M. H., & Ekers, R. D. 2001, *A&A*, **365**, 392
- Prandoni, I., Parma, P., Wieringa, M. H., de Ruiter, H. R., Gregorini, L., Mignano, A., Vettolani, G., & Ekers, R. D. 2006, *A&A*, **457**, 517
- Prandoni, I., Guglielmino, G., Morganti, R., Vaccari, M., Maini, A., Röttgering, H. J. A., Jarvis, M. J., & Garrett, M. A. 2018, *MNRAS*, **481**, 4548
- Predehl, P., et al. 2021, *A&A*, **647**, A1
- Quici, B., et al. 2021, *PASA*, **38**, e008
- Rau, U., & Cornwell, T. J. 2011, *A&A*, **532**, A71
- Rau, U., Bhatnagar, S., Voronkov, M. A., & Cornwell, T. J. 2009, *IEEE Proc.*, **97**, 1472
- Reiprich, T. H., et al. 2021, *A&A*, **647**, A2
- Rudnick, L. 2002, *PASP*, **114**, 427
- Sabater, J., et al. 2019, *A&A*, **622**, A17
- Saripalli, L., Subrahmanyam, R., Thorat, K., Ekers, R. D., Hunstead, R. W., Johnston, H. M., & Sadler, E. M. 2012, *ApJS*, **199**, 27
- Scheuer, P. A. G. 1957, *Proce. Cambridge Philos. Soc.*, **53**, 764
- Schilizzi, R. T., & McAdam, W. B. 1975, *MNRAS*, **79**, 1
- Siewert, T. M., et al. 2020, *A&A*, **643**, A100
- Tabatabaei, F. S., et al. 2017, *ApJ*, **836**, 185
- Taylor, M. B., 2005, in *Astronomical Society of the Pacific Conference Series*, vol. 347, *Astronomical Data Analysis Software and Systems XIV*, ed. P. Shopbell, M. Britton, & R. Ebert, 29
- Turner, R. J., Rogers, J. G., Shabala, S. S., & Krause, M. G. H. 2018, *MNRAS*, **473**, 4179
- Urry, C. M., & Padovani, P. 1995, *PASP*, **107**, 803
- Vernstrom, T., et al. 2014, *MNRAS*, **440**, 2791
- White, R. L., Becker, R. H., Helfand, D. J., & Gregg, M. D. 1997, *ApJ*, **475**, 479
- White, S. V., et al. 2020a, *PASA*, **37**, e017
- White, S. V., et al. 2020b, *PASA*, **37**, e018
- Whiting, M. T. 2020, in *Astronomical Data Analysis Software and Systems XXVII*, ed. P. Ballester, J. Ibsen, M. Solar, & K. Shorridge, *Astronomical Society of the Pacific Conference Series*, vol. 522, 469
- Whiting, M., & Humphreys, B. 2012, *PASA*, **29**, 371
- Whiting, M., Voronkov, M., Mitchell, D., & Askap Team, 2017, *Early Science Pipelines for ASKAP*, 431
- Whittam, I. H., et al. 2013, *MNRAS*, **429**, 2080
- Wilman, R. J., et al. 2008, *MNRAS*, **388**, 1335
- Wong, O. I., Meurer, G. R., Zheng, Z., Heckman, T. M., Thilker, D. A., & Zwaan, M. A. 2016, *MNRAS*, **460**, 1106
- Zhou, R., et al. 2021, *MNRAS*, **501**, 3309
- Zinn, P. C., Middelberg, E., Norris, R. P., Hales, C. A., Mao, M. Y., & Randall, K. E. 2012, *A&A*, **544**, A38
- Zou, H., Gao, J., Zhou, X., & Kong, X. 2019, *ApJS*, **242**, 8
- Zou, H., Gao, J., Zhou, X., & Kong, X. 2020, *VizieR Online Data Catalog*, J/ApJS/242/8
- van Weeren, R. J., de Gasperin, F., Akamatsu, H., Brügggen, M., Feretti, L., Kang, H., Stroe, A., & Zandanel, F. 2019, *SSRv*, **215**, 16